Coil-stretch transition in an ensemble of polymers in isotropic turbulence

Takeshi Watanabe* and Toshiyuki Gotoh
Graduate School of Engineering, Department of Scientific and Engineering Simulation, Nagoya Institute of Technology, Gokiso, Showa-ku, Nagoya 466-8555, Japan
and CREST, Japan Science and Technology Agency, 4-1-8 Honcho, Kawaguchi, Saitama 332-0012, Japan
(Received 5 March 2010; published 4 June 2010)

We study the statistical properties of ensembles of polymers in isotropic turbulence numerically in the one-way coupling regime. A linear polymer chain passively convected by turbulence is modeled by a line of beads, each of which is connected by a finitely extensible nonlinear elastic force and subject to Brownian motion. We find that when the Weissenberg number $\mathrm{Wi}_\eta < 1$, the polymer chain has a coiled configuration, while for $\mathrm{Wi}_\eta > 10$, it remains stretched for a much longer time than the typical time scale of the fluctuating turbulent velocity gradient. Various statistical quantities characterizing the ensemble of polymers, such as the mean, variance, autocorrelation time, and probability density function of the end-to-end vector distance, indicate that the coil-stretch transition occurs at $\mathrm{Wi}_\eta = 3-4$. We also find that this trend is insensitive to the number of beads N_b ($N_b=20$ or $N_b=2$), provided that the parameters in the model with a small number of beads are properly generated from the one with a large number of beads (i.e., using the formula of Jin and Collins). Finally, the Wi_η effects on the alignment of the end-to-end vector versus the principal axis of the rate of strain tensor and on the polymer elongation are examined from the viewpoint of local flow topology.

DOI: 10.1103/PhysRevE.81.066301 PACS number(s): 47.57.Ng, 47.27.ek, 83.10.Mj, 47.27.Gs

I. INTRODUCTION

The flow of a dilute polymer solution is peculiar when compared to that of a Newtonian fluid. One famous example is the drag reduction in wall-bounded turbulent flows, where the skin friction is significantly reduced by the addition of dilute polymers [1,2]. A remarkable flow property of dilute polymer solutions is also observed in low Reynolds number flow, which is the so-called elastic turbulence [3–5]. The elastic stress due to polymer additives plays an essential role in causing hydrodynamic instability (elastic instability) [6]. This phenomenon is used to enhance mixing in microchannel devices, in which the fluid velocity fluctuates randomly in space and time [7–9]. Although many experimental and numerical studies of polymer solution flow have been performed in recent years [10–13], the mechanism by which the polymer dynamics affects the macroscale fluid motion is not fully understood at present.

The "coil-stretch" (CS) transition is a key to understanding the dynamics of polymer chains in flows [14]. Many experimental, theoretical, and numerical studies have addressed the statistical nature of polymer dynamics in random [15–21], simple shear or laminar [22–25], and Navier-Stokes (NS) flows [26–33]. The probability density function (PDF) of the polymer extension is a good measure of the CS transition. Analytical PDF forms have been obtained by several groups [15–19,23]. The PDF of polymer elongation shows a power-law decay for moderate amplitudes. This decay law has been verified in an experimental study of single polymer dynamics in a random flow [20] and in direct numerical simulation (DNS) studies using a constitutive equation [26,27]. In addition, the relaxation time toward the stationary state, which increases rapidly near the CS transition point, has been discussed theoretically and numerically [18,19,21]. The tumbling time, which is defined as the time between two successive flips of the polymer, has also been discussed in simple shear flow cases [22,24]. The PDF of tumbling times shows exponential decay, with a decay rate that depends on the Weissenberg number (the ratio of the characteristic time of the polymer to that of the flow). However, all these results have been obtained in ideal flows or using a dumbbell model. Strain fields in turbulence fluctuate strongly, and our knowledge of the statistics and dynamics of polymer chains in realistic turbulent flows is very limited.

Let us consider the space and time scales of polymer and turbulent flow by following the case of experimental study [13]. The characteristic length of a polymer is estimated from the equilibrium radius of gyration $R_g = 0.5$ μm. The smallest scale in turbulent velocity fields is the Kolmogorov dissipation length of $\eta = (\nu^3/\bar{\epsilon})^{1/4} = 50$ μm, where ν is the kinematic viscosity and $\bar{\epsilon}$ is the rate of energy dissipation per unit mass, when the turbulent Reynolds number (based on the Taylor microscale) is $R_\lambda \sim 100$ [13]. Hence, the spatial scale disparity is $R_g/\eta \approx 10^{-2}$. However, the characteristic time of a polymer is the time τ_{re} for an elongated polymer to relax to the equilibrium state. The time scale of a turbulent flow in this context is the Kolmogorov time $\tau_\eta = (\nu/\bar{\epsilon})^{1/2}$. Unlike the length scale ratio, the characteristic time scale ratio $\mathrm{Wi}_\eta = \tau_{re}/\tau_\eta$ varies from very small to very large values, corresponding to time scales at the lower end of the inertial range.

This scale separation in space is the foundation of simple models of flow-polymer interaction. For example, in the limit $R_g/\eta \to 0$, a dumbbell model in a simple shear (or linear) flow and a constitutive equation model for additional stress terms in the NS equations may be used. In the former model, the strain field is quite often assumed to be constant. However, the persistence time of the strain field in turbulence is on the order of the Kolmogorov time, so that when $\mathrm{Wi}_\eta > 1$ the stationary strain field assumption becomes inad-

*watanabe@nitech.ac.jp

equate. This means that the strength and direction change appreciably during the deformation of the polymer configuration. Hence, the tumbling motion of the polymer could be changed by the turbulence. Moreover, the amplitude, direction, and persistence time of the strain field fluctuate intermittently in space and time, because a fluid blob containing polymers is convected and deformed under the action of strong turbulent fluctuations. These fluctuations are strongly non-Gaussian, especially at small scales. In addition, the spatial distribution of polymers in turbulent flow becomes spottier (intermittent), as inferred from recent studies of the dispersion of inertial particles in turbulence [34,35]. These considerations all suggest that the polymer dynamics in realistic turbulent flows may be significantly different from that obtained in idealized cases.

One way to obtain more insight into this problem is by direct solution of the motion of a large set of polymers with many degrees of freedom, with simultaneous solution for the turbulent flow field using a high performance computer. However, even with a state-of-the-art machine, it is not possible to resolve the motion of polymer and fluid atoms directly. Hence, we must introduce a model for the polymer degrees of freedom. Because our interest lies in the common features of the interaction between the long polymer chain and the flow, independent of the polymer type, it is quite reasonable to model the polymer as a large number of linearly connected particles (beads), with characteristics such as the number of particles, segment length, and interaction potential among particles all specified. Then the motions of the particles and fluid are simultaneously computed. This approach is a mesoscale-macroscale problem that involves many degrees of freedom with widely varying space and time scales. The approach is expensive, but it allows us to obtain more detailed knowledge of the statistical nature of polymer solutions in turbulent flow. In addition, it can increase our understanding of the CS transition and interactions between the polymer and flow, which are very important for constructing more physically motivated macroscopic equations to predict the motion of polymer solutions.

Our goal is to gain insight into polymer chain dynamics in turbulent flows using direct numerical simulation of many scales of motion, from mesoscale to macroscale. We focus on (i) the Wi_η dependency of the polymer chain dynamics in turbulent flow and (ii) the relationship between polymer elongation and local flow topology. We solve numerically a Brownian motion model of polymers that are passively advected (one-way coupling) by homogeneous isotropic turbulence (HIT). The HIT is generated by DNS of the NS equations with a random external force. We then examine the statistics and dynamics of polymers by changing Wi_η.

This paper is organized as follows. The governing equations for the polymer chain model and solvent velocity field are derived in Sec. II. Details of the numerical simulation, including the parameters used, are described in Sec. III. In Sec. IV, we discuss the statistical nature of the turbulent velocity field used to investigate the polymer dynamics and briefly examine the statistics of velocity gradient fluctuations in the Lagrangian frame. In Sec. V, we investigate the statistical nature of polymer elongation dynamics, with a special focus on the nature of the CS transition in turbulence. In Sec. VI, the relationship between the polymer elongation and local flow topology of the velocity gradient in HIT is investigated. We discuss the main results obtained in this study in Sec. VII.

II. MODELS FOR NUMERICAL SIMULATIONS

A. Fundamental equations for solvent fluids and polymers

The equation of motion of an incompressible solvent fluid is given by the NS equation

$$\frac{\partial \boldsymbol{u}}{\partial t} + \boldsymbol{u}\cdot\nabla\boldsymbol{u} = -\frac{1}{\rho_f}\nabla p + \nu\nabla^2\boldsymbol{u} + \boldsymbol{f}^e + \frac{1}{\rho_f}\boldsymbol{A}, \tag{1}$$

with the incompressibility condition

$$\nabla\cdot\boldsymbol{u} = 0, \tag{2}$$

where ρ_f, ν, and p are the fluid density, kinematic viscosity, and pressure, respectively. The term $\boldsymbol{f}^e$ denotes a solenoidal external force and $\boldsymbol{A}$ represents the backreaction from the beads composing the polymer chain (defined later).

We consider a bead-spring model for the polymer chain, which consists of N_b beads connected linearly by spring forces. We suppose that the Stokes drag and Brownian random forces $\boldsymbol{W}^{(n)}$ act on each bead due to the solvent fluid. Then the equations of motion of each bead of a single polymer are given by

$$\frac{d\boldsymbol{x}^{(n)}}{dt} = \boldsymbol{v}^{(n)}, \tag{3}$$

$$m_p\frac{d\boldsymbol{v}^{(n)}}{dt} = -\zeta[\boldsymbol{v}^{(n)} - \boldsymbol{u}(\boldsymbol{x}^{(n)}(t),t)] + \boldsymbol{F}^{(n)} + \boldsymbol{W}^{(n)}, \tag{4}$$

where $\boldsymbol{x}^{(n)}$ and $\boldsymbol{v}^{(n)}$ for $n=1,\ldots,N_b$ are the nth bead position and velocity vectors, respectively, and $\zeta=6\pi\nu\rho_f a$ for a spherical bead. The mass of bead m_p is given by $m_p=4\pi a^3\rho_p/3$, where a and ρ_p are the bead radius and density. $\boldsymbol{F}^{(n)}$ is the elastic force due to the spring connecting the nth and $(n\pm1)$th beads, i.e., $\boldsymbol{F}^{(n)}=\boldsymbol{F}^{(n)}(\boldsymbol{x}^{(n-1)},\boldsymbol{x}^{(n)},\boldsymbol{x}^{(n+1)})$, as defined in a later section. The fluctuation-dissipation theorem fixes the thermal random force $\boldsymbol{W}^{(n)}$ obeying Gaussian statistics as

$$\langle W_i^{(n)}\rangle = 0, \tag{5}$$

$$\langle W_i^{(m)}(t)W_j^{(n)}(s)\rangle = 2\zeta k_B T\delta_{ij}\delta_{mn}\delta(t-s), \tag{6}$$

where k_B is the Boltzmann constant, T is the temperature, and δ_{ij} is the Kronecker delta.

Because the relaxation time $\tau_p=m_p/\zeta$ of a bead in the solvent fluid is generally much shorter than the typical time scale of velocity fluctuations at small scales, we can neglect inertial term in Eq. (4). With this assumption, the equation of motion for the polymer is

$$\frac{d\boldsymbol{x}^{(n)}}{dt} = \boldsymbol{u}(\boldsymbol{x}^{(n)}(t),t) + \frac{1}{\zeta}(\boldsymbol{F}^{(n)} + \boldsymbol{W}^{(n)}). \tag{7}$$

The backreaction force $\boldsymbol{A}^{(l)}$ from lth single polymer chain to the fluid is expressed as

$$\boldsymbol{A}^{(l)}(\boldsymbol{x},t) = -\sum_{n=1}^{N_b} [\zeta\{\boldsymbol{u}[\boldsymbol{x}^{(n)},t] - \boldsymbol{v}^{(n)}\} + \boldsymbol{W}^{(n)}]\delta[\boldsymbol{x} - \boldsymbol{x}^{(n)}], \tag{8}$$

which becomes

$$\boldsymbol{A}^{(l)}(\boldsymbol{x},t) = \sum_{n=1}^{N_b} \boldsymbol{F}^{(n)}(\boldsymbol{x}^{(n-1)},\boldsymbol{x}^{(n)},\boldsymbol{x}^{(n+1)})\,\delta(\boldsymbol{x} - \boldsymbol{x}^{(n)}) \tag{9}$$

when the inertial effect is neglected.

B. Elastic force model

The finitely extensible nonlinear elastic (FENE) formulation [36] is used for the elastic force $\boldsymbol{F}^{(n)}$ in the bead-spring model. This is given by

$$\boldsymbol{F}^{(n)} = -\frac{k(\boldsymbol{x}^{(n)} - \boldsymbol{x}^{(n+1)})}{1 - (|\boldsymbol{x}^{(n)} - \boldsymbol{x}^{(n+1)}|/r_{max})^2} - \frac{k(\boldsymbol{x}^{(n)} - \boldsymbol{x}^{(n-1)})}{1 - (|\boldsymbol{x}^{(n)} - \boldsymbol{x}^{(n-1)}|/r_{max})^2}, \tag{10}$$

where k and r_{max} are the spring constant and maximum extension of the spring, respectively. The restoring force diverges as the separation distance $|\boldsymbol{x}^{(n)} - \boldsymbol{x}^{(n-1)}|$ approaches r_{max}. This means that the separation distance cannot exceed r_{max}. Introducing connector vectors $\boldsymbol{r}^{(n)} = \boldsymbol{x}^{(n+1)} - \boldsymbol{x}^{(n)}$, we rewrite Eq. (10) as

$$\boldsymbol{F}^{(n)} = k\left[f\left(\frac{r^{(n)}}{r_{max}}\right)\boldsymbol{r}^{(n)} - f\left(\frac{r^{(n-1)}}{r_{max}}\right)\boldsymbol{r}^{(n-1)}\right], \tag{11}$$

with $f(z) \equiv (1 - z^2)^{-1}$. Hereafter, we use $f_n = f(r^{(n)}/r_{max})$ for brevity.

C. Variable transformation and normalization

Equation (7) can be rewritten in terms of the center of bead position vector $\boldsymbol{x}^g(t) = N_b^{-1}\Sigma_{n=1}^{N_b}\boldsymbol{x}^{(n)}(t)$ and the connector vectors $\boldsymbol{r}^{(n)}(t)$ as

$$\frac{d\boldsymbol{x}^g}{dt} = \frac{1}{N_b}\sum_{n=1}^{N_b} \boldsymbol{u}(\boldsymbol{x}^{(n)}) + \frac{1}{\zeta}\boldsymbol{W}^g, \tag{12}$$

$$\frac{d\boldsymbol{r}^{(n)}}{dt} = \boldsymbol{u}(\boldsymbol{x}^{(n+1)}(t)) - \boldsymbol{u}(\boldsymbol{x}^{(n)}(t)) + \frac{k}{\zeta}[f_{n+1}\boldsymbol{r}^{(n+1)} + f_{n-1}\boldsymbol{r}^{(n-1)} - 2f_n\boldsymbol{r}^{(n)}] + \frac{1}{\zeta}(\boldsymbol{W}^{(n+1)} - \boldsymbol{W}^{(n)}), \tag{13}$$

where $\boldsymbol{W}^g \equiv N_b^{-1}\Sigma_{n=1}^{N_b}\boldsymbol{W}^{(n)}$. When we define $\boldsymbol{\rho}^{(n)} \equiv \boldsymbol{x}^{(n)} - \boldsymbol{x}^g$ and $\boldsymbol{r}^{(n)} = \boldsymbol{\rho}^{(n+1)} - \boldsymbol{\rho}^{(n)}$, and when the maximum linear size of the most elongated polymer is smaller than the typical length scale of the velocity field (Kolmogorov scale $\sim\eta$), we can expand $\boldsymbol{u}(\boldsymbol{x}^{(n)})$ around $\boldsymbol{x}^g$ as

$$u_i(\boldsymbol{x}^{(n)}) = u_i(\boldsymbol{x}^g) + \frac{\partial u_i(\boldsymbol{x}^g)}{\partial x_j}\rho_j^{(n)} + O(|\boldsymbol{\rho}^{(n)}|^2), \tag{14}$$

where the summation convention for repeated indices is used. Using Eq. (14), we approximate the velocity terms from the solvent fluid motion as

$$\frac{1}{N_b}\sum_{n=1}^{N_b} \boldsymbol{u}(\boldsymbol{x}^{(n)}) \simeq \boldsymbol{u}(\boldsymbol{x}^g(t)), \tag{15}$$

$$\boldsymbol{u}(\boldsymbol{x}^{(n+1)}(t)) - \boldsymbol{u}(\boldsymbol{x}^{(n)}(t)) \simeq \frac{\partial u_i(\boldsymbol{x}^g(t))}{\partial x_j} r_j^{(n)}. \tag{16}$$

Substituting Eqs. (15) and (16) into Eqs. (12) and (13) yields

$$\frac{d\boldsymbol{x}^g}{dt} = \boldsymbol{u}(\boldsymbol{x}^g) + \frac{1}{\zeta}\boldsymbol{W}^g, \tag{17}$$

$$\frac{d\boldsymbol{r}^{(n)}}{dt} = \boldsymbol{r}^{(n)} \cdot \boldsymbol{\nabla}\boldsymbol{u}(\boldsymbol{x}^g) + \frac{k}{\zeta}[f_{n+1}\boldsymbol{r}^{(n+1)} + f_{n-1}\boldsymbol{r}^{(n-1)} - 2f_n\boldsymbol{r}^{(n)}] + \frac{1}{\zeta}(\boldsymbol{W}^{(n+1)} - \boldsymbol{W}^{(n)}). \tag{18}$$

Under the assumption $r_{max} \ll \eta$, the contribution to the fluid from the lth polymer chain whose center of mass is at $\boldsymbol{x}_l^g$ becomes

$$A_i^{(l)}(\boldsymbol{x},t) = k\frac{\partial}{\partial x_j}\left[\sum_{m=1}^{N_b-1} r_i^{(m)} r_j^{(m)} f_m \delta(\boldsymbol{x} - \boldsymbol{x}_l^g)\right]. \tag{19}$$

We rewrite the NS equation by introducing the nondimensional variables

$$\tilde{\boldsymbol{u}} = \boldsymbol{u}/\mathcal{U}, \quad \tilde{\boldsymbol{x}} = \boldsymbol{x}/\mathcal{L}, \quad \tilde{t} = t/\mathcal{T}, \quad \tilde{p} = p/(\rho_f \mathcal{U}^2), \tag{20}$$

as follows:

$$\tilde{\boldsymbol{\nabla}} \cdot \tilde{\boldsymbol{u}} = 0, \tag{21}$$

$$\frac{\partial \tilde{\boldsymbol{u}}}{\partial \tilde{t}} + \tilde{\boldsymbol{u}} \cdot \tilde{\boldsymbol{\nabla}}\tilde{\boldsymbol{u}} = -\boldsymbol{\nabla}\tilde{p} + \frac{1}{\mathrm{Re}}\tilde{\nabla}^2\tilde{\boldsymbol{u}} + \tilde{\boldsymbol{f}}^e + \tilde{\boldsymbol{A}}, \tag{22}$$

where $\mathcal{L}$, $\mathcal{U}$, and $\mathcal{T} = \mathcal{L}/\mathcal{U}$ are the characteristic length, velocity scales, and time scale of the fluid motion, respectively, and $\mathrm{Re} = \mathcal{U}\mathcal{L}/\nu$ is the Reynolds number. The external force $\tilde{\boldsymbol{f}}^e$ and the reaction from the beads $\tilde{\boldsymbol{A}}$ are, respectively, normalized by $\mathcal{L}/\mathcal{U}^2$ and $\mathcal{L}/(\rho_f\mathcal{U}^2)$. The governing equations of the polymer chain model are normalized using the variables

$$\tilde{\boldsymbol{x}}^g = \boldsymbol{x}^g/\mathcal{L}, \quad \tilde{\boldsymbol{r}}^{(n)} = \boldsymbol{r}^{(n)}/r_{eq}, \quad \tilde{\boldsymbol{W}}^{(n)} = \boldsymbol{W}^{(n)}\sqrt{\frac{\mathcal{T}}{2\zeta k_B T}}, \tag{23}$$

where the polymer equilibrium length r_{eq} is defined by

$$r_{eq} \equiv \left(\frac{k_B T}{k}\right)^{1/2}. \tag{24}$$

Then Eqs. (17) and (18) are rewritten as

$$\frac{d\tilde{\boldsymbol{x}}^g}{d\tilde{t}} = \tilde{\boldsymbol{u}}(\tilde{\boldsymbol{x}}^g) + \frac{r_{eq}}{\mathcal{L}}\frac{1}{\sqrt{2\tilde{\tau}_s}}\tilde{\boldsymbol{W}}^g, \tag{25}$$

$$\frac{d\tilde{\boldsymbol{r}}^{(n)}}{d\tilde{t}} = \tilde{\boldsymbol{r}}^{(n)} \cdot \tilde{\boldsymbol{\nabla}}\tilde{\boldsymbol{u}}(\tilde{\boldsymbol{x}}^g) + \frac{1}{4\tilde{\tau}_s}[f_{n+1}\tilde{\boldsymbol{r}}^{(n+1)} + f_{n-1}\tilde{\boldsymbol{r}}^{(n-1)} - 2f_n\tilde{\boldsymbol{r}}^{(n)}] + \frac{1}{\sqrt{2\tilde{\tau}_s}}(\tilde{\boldsymbol{W}}^{(n+1)} - \tilde{\boldsymbol{W}}^{(n)}), \tag{26}$$

where $\tilde{\tau}_s = \tau_s/\mathcal{T}$ is the normalized characteristic time scale for a segment of the polymer chain and

$$\tau_s = \frac{\zeta}{4k}. \tag{27}$$

The thermal random force Eq. (6) is also rewritten as

$$\langle \tilde{W}_i^{(n)} \rangle = 0, \tag{28}$$

$$\langle \tilde{W}_i^{(m)}(\tilde{t})\tilde{W}_j^{(n)}(\tilde{s})\rangle = \delta_{ij}\delta_{mn}\delta(\tilde{t}-\tilde{s}). \tag{29}$$

The backreaction force from the lth single polymer [Eq. (19)] is represented as

$$\tilde{A}_i^{(l)}(\tilde{\boldsymbol{x}},\tilde{t}) = A_0\frac{\partial}{\partial\tilde{x}_j}\left[\sum_{m=1}^{N_b-1}\tilde{r}_i^{(m)}\tilde{r}_j^{(m)}f_m\delta(\tilde{\boldsymbol{x}}-\tilde{\boldsymbol{x}}_l^g)\right],$$

$$A_0 = \frac{3\pi}{2\tilde{\tau}_s\,\mathrm{Re}}\left(\frac{ar_{eq}^2}{\mathcal{L}^3}\right). \tag{30}$$

D. Polymer stress tensor

The polymer stress tensor is computed in the following way. Suppose that there are $N_c(\tilde{\boldsymbol{x}},\tilde{t})$ polymers in a small volume (for example, the grid volume $\Delta\tilde{x}^3$) centered at $\tilde{\boldsymbol{x}}$ at time $\tilde{t}$ in the flow. The total reaction force from the polymers $\tilde{A}_i(\tilde{\boldsymbol{x}},\tilde{t})$ at $\tilde{\boldsymbol{x}}$ and $\tilde{t}$ is given by summing contributions from all polymers,

$$\tilde{A}_i(\tilde{\boldsymbol{x}},\tilde{t}) = \sum_{l=1}^{N_c(\tilde{\boldsymbol{x}},\tilde{t})}\tilde{A}_i^{(l)}(\tilde{\boldsymbol{x}},\tilde{t}) = A_0\frac{\partial}{\partial\tilde{x}_j}\sum_{l=1}^{N_c(\tilde{\boldsymbol{x}},\tilde{t})}\left[\sum_{m=1}^{N_b-1}\tilde{r}_i^{(m)}(\tilde{\boldsymbol{x}}_l^g)\tilde{r}_j^{(m)}(\tilde{\boldsymbol{x}}_l^g)f_m(\tilde{\boldsymbol{x}}_l^g)\delta(\tilde{\boldsymbol{x}}-\tilde{\boldsymbol{x}}_l^g)\right]. \tag{31}$$

When the number of polymers within the unit cell is large but small enough for the interaction among polymers to be neglected, and the polymers are assumed to be homogeneously distributed in the cell, the summation of the delta functions over the number of polymers can be approximated by the local number density such that $\sum_{l=1}^{N_c(\tilde{\boldsymbol{x}},\tilde{t})}\delta(\tilde{\boldsymbol{x}}-\tilde{\boldsymbol{x}}_l^g) \approx n(\tilde{\boldsymbol{x}},\tilde{t})$. Then Eq. (31) is approximated by

$$\tilde{A}_i(\tilde{\boldsymbol{x}},\tilde{t}) \approx A_0\frac{\partial}{\partial\tilde{x}_j}\sum_{l=1}^{N_c(\tilde{\boldsymbol{x}},\tilde{t})}\left[\sum_{m=1}^{N_b-1}\tilde{r}_i^{(m)}(\tilde{\boldsymbol{x}}_l^g)\tilde{r}_j^{(m)}(\tilde{\boldsymbol{x}}_l^g)f_m(\tilde{\boldsymbol{x}}_l^g)\right]\Delta\tilde{x}^{-3} \tag{32}$$

$$\approx A_0\frac{\partial}{\partial\tilde{x}_j}\tilde{n}(\tilde{\boldsymbol{x}},\tilde{t})\left\langle\sum_{m=1}^{N_b-1}\tilde{r}_i^{(m)}(\tilde{\boldsymbol{x}}_l^g)\tilde{r}_j^{(m)}(\tilde{\boldsymbol{x}}_l^g)f_m(\tilde{\boldsymbol{x}}_l^g)\right\rangle_{N_p(\tilde{\boldsymbol{x}},\tilde{t})}, \tag{33}$$

where $\langle\cdots\rangle_{N_p}$ represents the average over the polymer configurations within the unit cell $\Delta\tilde{x}^3$, and $\tilde{n}(\tilde{\boldsymbol{x}},\tilde{t}) = N_c(\tilde{\boldsymbol{x}},\tilde{t})/\Delta\tilde{x}^3$ (note that $n = N_c/\Delta x^3 = \tilde{n}/\mathcal{L}^3$) is the number density of the polymer. Then the nondimensional polymer stress tensor $\tilde{T}_{ij}^p$ is defined by

$$\tilde{T}_{ij}^p(\tilde{\boldsymbol{x}},\tilde{t}) = A_0\tilde{n}(\tilde{\boldsymbol{x}},\tilde{t})\left[\left\langle\sum_{m=1}^{N_b-1}\tilde{r}_i^{(m)}(\tilde{\boldsymbol{x}}_l^g)\tilde{r}_j^{(m)}(\tilde{\boldsymbol{x}}_l^g)f_m(\tilde{\boldsymbol{x}}_l^g)\right\rangle_{N_p(\tilde{\boldsymbol{x}},\tilde{t})} - (N_b-1)\delta_{ij}\right], \tag{34}$$

so that the backreaction term (33) is related to the polymer stress tensor as

$$\tilde{A}_i(\tilde{\boldsymbol{x}},\tilde{t}) = \frac{\partial}{\partial\tilde{x}_j}\tilde{T}_{ij}^p. \tag{35}$$

The factor in Eq. (34) is rewritten as

$$A_0\tilde{n}(\tilde{\boldsymbol{x}},\tilde{t}) = \frac{3\pi}{2\tilde{\tau}_s\,\mathrm{Re}}\left(\frac{ar_{eq}^2}{\mathcal{L}^3}\right)\tilde{n}(\tilde{\boldsymbol{x}},\tilde{t}). \tag{36}$$

It is useful to estimate the magnitude of the term $A_0\tilde{n}$. The average volume fraction of a polymer is $\phi_0 = (4\pi a^3N_b/3)n_0 \approx (4\pi a^3N_b/3)(\tilde{n}_0/\mathcal{L}^3)$. The normalized time scale of the bead is $\tilde{\tau}_s = \tau_s/\mathcal{T} = \mathrm{Wi}_\eta^{seg}\,\tau_\eta/\mathcal{T} \sim \mathrm{Wi}_\eta^{seg}\,\mathrm{Re}^{-1/2}$, where $\mathrm{Wi}_\eta^{seg} = \tau_s/\tau_\eta$ is the Weissenberg number for a segment. This allows us to estimate the average amplitude of the reaction from the polymers as

$$A_0n_0 \sim \frac{\phi_0}{N_b}\left(\frac{r_{eq}}{2a}\right)^2\frac{1}{R_\lambda\,\mathrm{Wi}_\eta^{seg}}, \tag{37}$$

where $R_\lambda(\propto\mathrm{Re}^{1/2})$ is the Taylor microscale Reynolds number. As we will see in the next section [see Eq. (44)], the overall relaxation time τ_D for a single polymer may be estimated as $\tau_D \propto N_b^2\tau_s$ for $N_b \gg 1$, and the Weissenberg number for the polymer becomes $\mathrm{Wi}_\eta \sim N_b^2\,\mathrm{Wi}_\eta^{seg}$. Therefore, Eq. (37) is expressed in terms of the Weissenberg number as

$$A_0n_0 \sim \phi_0\left(\frac{r_{eq}}{2a}\right)^2\frac{N_b}{R_\lambda\,\mathrm{Wi}_\eta}. \tag{38}$$

The reaction is proportional to the volume fraction. The ratio $r_{eq}/2a$ is a parameter that is expected to be of order unity. For given Reynolds and Weissenberg numbers, the reaction force from the ensemble of polymers is proportional to the volume fraction ϕ_0 and N_b. When the number of polymer segments is very large and the polymer is in the strong straining domain of turbulent flow, the polymer chain is so highly extended that $r^{(n)}/r_{max}$ remains close to unity. Hence, if N_b is large enough to compensate $R_\lambda\,\mathrm{Wi}_\eta$ in the denominator while keeping ϕ_0 almost unchanged (this is possible because the polymer is a one-dimensional object embedded in the three-dimensional space), then the reactive force from

the polymer to the fluid motion becomes appreciable. In other words, the above estimate suggests that larger strain and longer chains imply a stronger reactive force from the polymer. In the analysis presented in this paper, we assume that the concentration of the polymer chain is very low and N_b is low, so the reaction from the polymers can be neglected.

III. NUMERICAL SIMULATION

We now describe the numerical scheme and conditions for the polymers in turbulent flow. The reaction from the polymers was neglected in this analysis (one-way coupling regime). Statistically homogeneous isotropic turbulence in an incompressible Newtonian fluid is numerically generated by solving the NS equations (22) and the continuity equation (21) in a cubic box with periodicity 2π. Hereafter, for brevity, we omit the overtilde used for the nondimensional variables.

To maintain the turbulence in a statistically steady state, a random external force $\boldsymbol{f}^e$ that is Gaussian and white in time was added. The mean and variance were

$$\langle f_i^e(\boldsymbol{x},t)\rangle = 0, \tag{39}$$

$$\langle f_i^e(\boldsymbol{x},t) f_j^e(\boldsymbol{x}',s)\rangle = F^e(|\boldsymbol{x}-\boldsymbol{x}'|)\,\delta_{ij}\Delta(t-s), \tag{40}$$

where $F^e(|\boldsymbol{x}-\boldsymbol{x}'|)$ is a function with spectral support in a low wave-number range in Fourier space. $\Delta(t)$ is the coarse-grained delta function in the time scale of NS equation. Equations (21) and (22) were solved using the pseudospectral method in space and the fourth-order Runge-Kutta-Gill method in time. The number of grids for the DNS was $N_g = 128^3$, and the temporal integration was performed for $T_{total}=52.8T_{eddy}=385\tau_\eta$, where T_{eddy} is the large eddy turnover time defined by $T_{eddy}\equiv L/u_{rms}$, L is the integral scale, $u_{rms}=\sqrt{\langle u_i^2\rangle/3}$, and τ_η is the Kolmogorov time. The Taylor microscale Reynolds number $R_\lambda = u_{rms}\lambda_T/\nu$ was 47, where λ_T is the Taylor microscale. The resolution condition was $k_{max}\eta=4.2$, where k_{max} is the truncation wave number and η is the Kolmogorov scale. This was sufficient to allow accurate computation of the velocity gradient field under strongly turbulent conditions [37].

We assumed that N_t polymers were introduced in the flow field and randomly distributed over the DNS computational domain. The polymers were convected and deformed due to the turbulence. The dynamics of each polymer solved in the fluid were expressed by

$$\frac{d\boldsymbol{x}_l^g}{dt} = \boldsymbol{u}(\boldsymbol{x}_l^g(t),t), \tag{41}$$

$$\frac{d\boldsymbol{r}_l^{(n)}}{dt} = \boldsymbol{r}_l^{(n)}\cdot\nabla\boldsymbol{u}(\boldsymbol{x}_l^g) + \frac{1}{4\tau_s(N_b)}[f_{n+1}\boldsymbol{r}_l^{(n+1)} + f_{n-1}\boldsymbol{r}_l^{(n-1)} - 2f_n\boldsymbol{r}_l^{(n)}] + \frac{1}{\sqrt{2\tau_s(N_b)}}(\boldsymbol{W}_l^{(n+1)} - \boldsymbol{W}_l^{(n)}), \quad \text{for } l = 1,2,\ldots,N_t. \tag{42}$$

In Eq. (41), we neglect Brownian random force because $r_{eq}/\mathcal{L} \ll 1$. The number of beads in a single polymer chain was chosen to be $N_b=20$, and the results were compared with those of the dumbbell model ($N_b=2$). To obtain meaningful comparison between the $N_b=2$ and $N_b=20$ cases, we needed a theoretical relationship between the spring parameters τ_s, r_{max}, and the bead number N_b. Here, we adopted the mapping formula proposed by Jin and Collins [32], where

$$r_{max}^2(N_b) = \frac{L_D^2}{N_b-1}, \tag{43}$$

$$\tau_s(N_b) = \frac{6\tau_D}{N_b(N_b+1)}. \tag{44}$$

We chose $L_D^2=3000$, also following [32]. τ_D was determined from the Weissenberg number Wi_η and τ_η [see Eq. (45)]. The Brownian dynamics simulation (BDS) for the polymer chain was performed using a second-order Runge-Kutta scheme with changing Weissenberg number Wi_η based on τ_η, which was defined by

$$\mathrm{Wi}_\eta = \frac{\tau_D}{\tau_\eta}, \tag{45}$$

as $\mathrm{Wi}_\eta=0.02-100$.

To numerically integrate the polymer chain model equations, it is necessary to track the velocity gradient $\nabla\boldsymbol{u}$ along the Lagrangian trajectory of N_t fluid particles, in addition to performing the DNS of the NS equation. Equation (41) was integrated in time for $N_t=256$ polymers. A trilinear interpolation scheme was used to obtain the velocity vector $u_i(\boldsymbol{x}^g)$ and the velocity gradient tensor $\partial_j u_i(\boldsymbol{x}^g)$ at the particle position from the grid data $u_i(\boldsymbol{x})$ and $\partial_j u_i(\boldsymbol{x})$. As we considered a one-way coupling regime, the N_t Lagrangian time series of these fluid quantities was computed and stored during T_{total}, and then used to integrate Eq. (42).

The polymer chain tends to be fully extended when Wi_η is large, meaning that the distance between adjacent beads is very close to the maximum extension length r_{max}. This causes numerically inaccurate results, because the restoring force is very large when $|\boldsymbol{r}^{(n)}| \sim r_{max}$. To avoid blowup of the temporal integration for $\mathrm{Wi}_\eta \gg 1$, it is necessary to keep the time increment small compared to that for $\mathrm{Wi}_\eta \simeq 1$. Therefore, the value of Δt_{BDS} used in the integral of the polymer chain was decreased as Wi_η increased, such that $\Delta t_{DNS}/\Delta t_{BDS} = O(1) \sim O(10^3)$. The time series of the Lagrangian velocity gradient at time t in the interval $n\Delta t_{DNS} \le t < (n+1)\Delta t_{DNS}$ was interpolated linearly. All the statistical data shown in this paper were computed by averaging over the integration time T_{total} and the total number of polymer chains N_t.

IV. LAGRANGIAN STATISTICS OF VELOCITY GRADIENTS

In this section, we examine the statistics of the velocity gradient fluctuations along the fluid particle trajectories. Figure 1 shows an example of a fluid particle trajectory during the temporal evolution of $200\tau_\eta$. The fluid particle moved

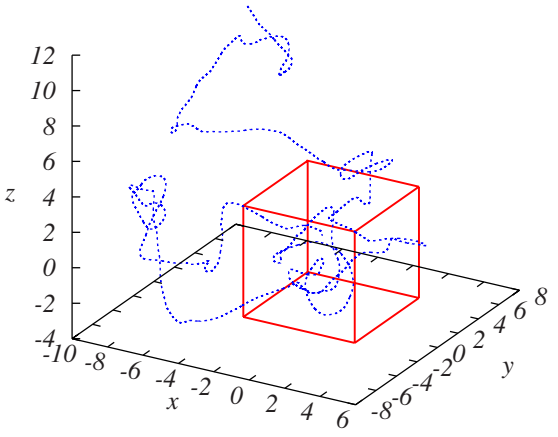

FIG. 1. (Color online) Example of a fluid particle trajectory tracked in the turbulence DNS with a duration of $200\tau_\eta$. The box plotted by solid line represents the computational domain $(2\pi)^3$.

around randomly, implying that the local structures of intense strain or vortices affected the fluid particle trajectory, even in the low R_λ case, so that the strain field experienced by the fluid particle fluctuated strongly.

To show the gradient field fluctuations in the Lagrangian frame, the temporal evolution of the rate of strain tensor S_{ij} and rate of rotation tensor Ω_{ij}, which are defined by the decomposition of velocity gradient tensor A_{ij} as

$$A_{ij} \equiv \frac{\partial u_j}{\partial x_i} = S_{ij} + \Omega_{ij}, \tag{46}$$

where

$$S_{ij} \equiv \frac{1}{2}\left(\frac{\partial u_j}{\partial x_i} + \frac{\partial u_i}{\partial x_j}\right), \quad \Omega_{ij} \equiv \frac{1}{2}\left(\frac{\partial u_j}{\partial x_i} - \frac{\partial u_i}{\partial x_j}\right), \tag{47}$$

are shown in Fig. 2. Both S_{ij} and Ω_{ij} fluctuated randomly and intermittently. Comparison of the temporal fluctuations between S_{ij} and Ω_{ij} showed that the characteristic time scale of S_{ij} was shorter than that of Ω_{ij}. The PDFs and time series for local energy dissipation along fluid particles based on the rate of strain tensor $\epsilon(t)=2\nu S_{ij}S_{ij}$ and vorticity vector $\Omega(t)=\nu\omega_i^2/2$ are shown in Fig. 3. Although the turbulence Reynolds number was too low to observe the inertial range, the Lagrangian time series of the energy dissipation indicated strong temporal intermittency, suggesting that the dissipation field was governed by the intermittent structure of intense vortices and the strain field. Intermittency also caused the long tails of the PDF, where the fluctuation of Ω was more intermittent than that of ϵ. The inset of Fig. 3 also shows that the time scale of fluctuating $\epsilon(t)$ was shorter than that of $\Omega(t)$.

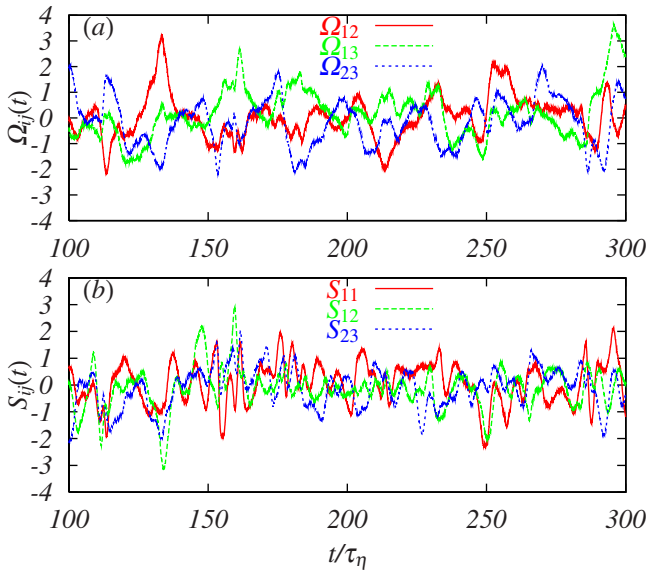

FIG. 2. (Color online) Lagrangian time evolution of (a) Ω_{ij} and (b) S_{ij}.

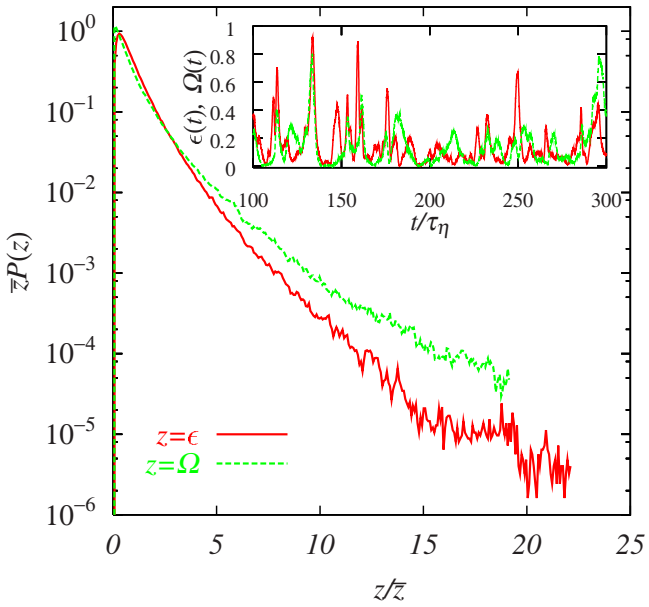

FIG. 3. (Color online) PDFs for the local energy dissipation fluctuation of $\epsilon(t)=2\nu S_{ij}S_{ij}$ and $\Omega(t)=\nu\omega_i^2/2$. Inset figure shows the Lagrangian time series of $\epsilon(t)$ and $\Omega(t)$ along the same fluid particle within $100\leq t/\tau_\eta\leq 300$.

Lagrangian autocorrelation functions $C_z(t)=\langle[z(t+t_0)-\langle z\rangle][z(t_0)-\langle z\rangle]\rangle$ ($z=A$, S, and Ω) of A_{ij}, S_{ij}, and Ω_{ij} computed from the time series are shown in Fig. 4. The correlation function for S_{ij} decreased more rapidly than that for Ω_{ij}, while the curve of A_{ij} was midway between those of S_{ij} and Ω_{ij}. When the characteristic correlation time was defined by the integral time $T_z=\int_0^\infty C_z(t)/C_z(0)dt$, we evaluated the correlation time as $T_A=4.3\tau_\eta$, $T_S=2.1\tau_\eta$, and $T_\Omega=6.6\tau_\eta$, so that $T_\Omega>T_S$. These results are largely consistent with those of previous study [38].

Other features of the velocity gradient statistics were obtained by examining the distribution of the three eigenvalues of the rate of strain tensor S_{ij}. The PDFs for three real eigenvalues σ_j ($j=1,2,3$) with $\sigma_1>\sigma_2>\sigma_3$ obtained in the Lagrangian frame are shown in Fig. 5. We can see that σ_1 (σ_3) had positive (negative) values, while σ_2 was both positive and negative. The PDF form for σ_2 was positively skewed. The mean eigenvalues were $\bar{\sigma}_1=1.164$, $\bar{\sigma}_2=0.283$, and $\bar{\sigma}_3=-1.447$. The PDF forms are very similar to those obtained in previous studies [39], although the detailed form depended

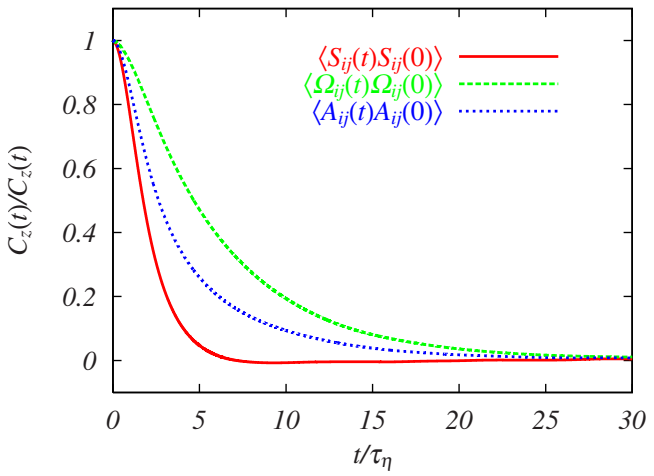

FIG. 4. (Color online) Lagrangian autocorrelation functions for the rate of strain tensor S_{ij}, for the rate of rotation tensor Ω_{ij}, and for the velocity gradient tensor $A_{ij}=S_{ij}+\Omega_{ij}$.

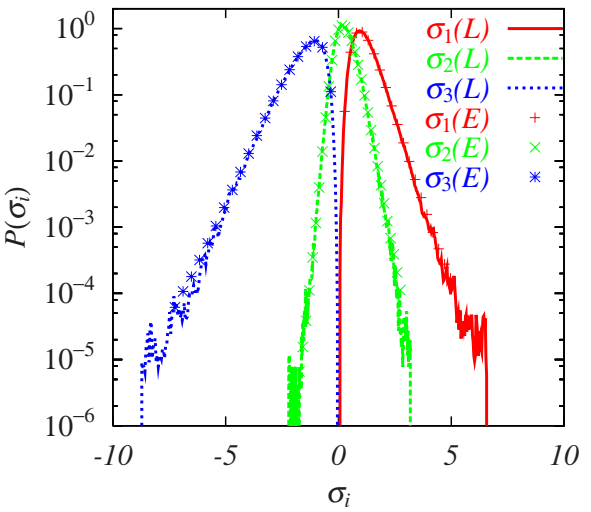

FIG. 5. (Color online) PDFs for three eigenvalues of the rate of strain tensor S_{ij}. $\sigma_i(L)$'s are evaluated from the data obtained in the Lagrangian frame, while $\sigma_i(E)$'s are calculated from data obtained in the Eulerian frame (DNS data on grid).

on R_λ. The functional forms of the PDFs obtained from Lagrangian data are very close to those obtained from Eulerian data (using the data set of the velocity gradient on the grid), indicating that the trilinear interpolation worked very well, even for the derivative statistics, at this resolution.

V. STATISTICS OF SINGLE POLYMER DYNAMICS

We performed the BDS of the polymer chain model using the Lagrangian time series of velocity gradients obtained

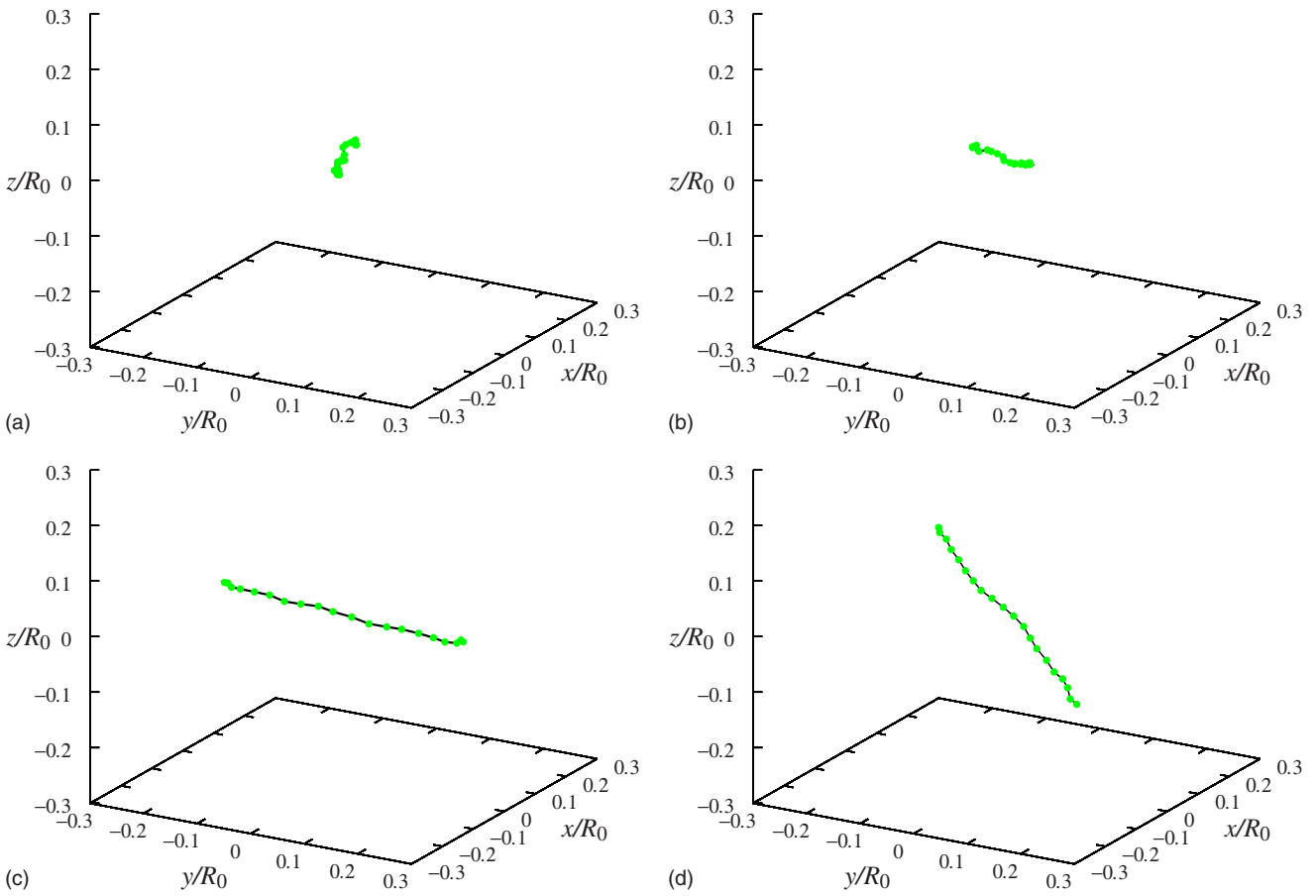

FIG. 6. (Color online) An example of the temporal evolution [from (a) to (d)] of the polymer elongation dynamics ($N_b=20$) in the case of $\mathrm{Wi}_\eta=4$. The time interval among the four figures is $3.7\tau_\eta$.

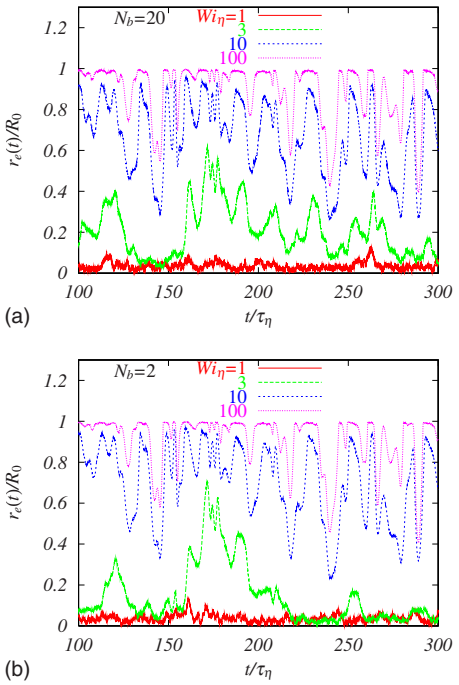

FIG. 7. (Color online) Time series of the end-to-end distance $|\boldsymbol{r}_e|$ normalized by the maximum extension length for (a) $N_b=20$ and (b) $N_b=2$ for $\mathrm{Wi}_\eta=1$, 3, 10, and 100.

from the DNS of isotropic turbulence. Figure 6 shows an example of the temporal evolution of a polymer chain configuration for $\mathrm{Wi}_\eta=4$ with $N_b=20$. The polymer chain, which was in a coiled state [Fig. 6(a)], was gradually extended while rotating under the influence of the Lagrangian dynamics of the velocity gradient. The stretched polymer again relaxed to a coiled state in a complex manner, which was in sharp contrast to the case for the dumbbell model ($N_b=2$).

We now discuss the statistical nature of polymer elongation and the folding dynamics in turbulent flow. An important "order parameter" to characterize the polymer dynamics is the end-to-end vector $\boldsymbol{r}_e$ of the polymer chain, which is defined by

$$\boldsymbol{r}_e = \boldsymbol{x}_{N_b} - \boldsymbol{x}_1 = \sum_{n=1}^{N_b-1} \boldsymbol{r}^{(n)}. \tag{48}$$

Figure 7 shows the time series of the end-to-end distance $|\boldsymbol{r}_e|$ normalized by the maximum extension length $R_0 \equiv (N_b-1)r_{max}$ for various Wi_η values. Although the polymer chain remained coiled over long time periods when $\mathrm{Wi}_\eta=1$, it occasionally extended as Wi_η increased. When $\mathrm{Wi}_\eta=100$, the polymer chain remained fully extended over a much longer time than the correlation time of the velocity gradient fluctuation. The temporal evolution for a polymer chain $N_b=20$ was also compared with the dumbbell case ($N_b=2$). The time series for $N_b=2$ was very close to that for $N_b=20$, even when $\mathrm{Wi}_\eta=10$. This suggests that the overall nature of the polymer chain for high Wi_η is approximately reproduced by the dumbbell model. The difference in behavior between $N_b=20$ and $N_b=2$ was significant when $\mathrm{Wi}_\eta \leq 3$, for which the polymer chain repeatedly extended and refolded. Because

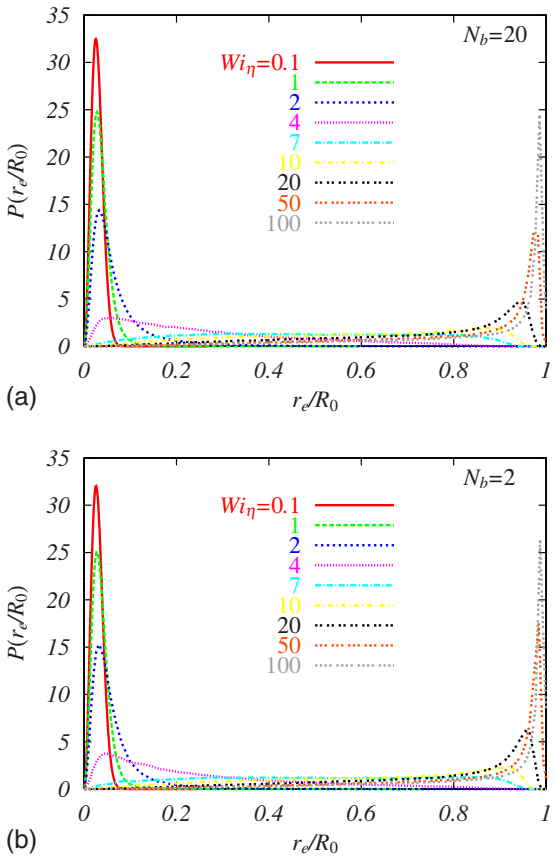

FIG. 8. (Color online) PDFs of the end-to-end distance $|\boldsymbol{r}_e|$ normalized by the maximum extension length for (a) $N_b=20$ and (b) $N_b=2$ for $\mathrm{Wi}_\eta=0.1-100$.

the polymer chain has a distribution of relaxation times, in contrast to the dumbbell model, which has a single relaxation time, the ways to refold into the coiled state became more complex when N_b was larger.

The PDF of $|\boldsymbol{r}_e|$ normalized by R_0 is shown in Fig. 8. The peak position of the PDF for $\mathrm{Wi}_\eta=0.1$ was located near $r_e/R_0=0$, and it increased with Wi_η. The polymer chain was almost fully extended when $\mathrm{Wi}_\eta=100$. Thus, it underwent a CS transition when Wi_η was increased. Remarkably, the PDF form for $N_b=20$ was very close to that for $N_b=2$, even when Wi_η was low to moderate. To investigate this point in more detail, various PDF curves are plotted on a logarithmic scale in Fig. 9. The curves obtained for both $N_b=20$ and $N_b=2$ for the same Wi_η values were almost identical for a wide range of elongation. This suggests that the dumbbell model can potentially describe polymer chain properties in the statistical sense. Figure 9(a) also shows that each PDF curve in the range $0.4 < r_e/R_0 < 0.8$ was approximately exponential, irrespective of Wi_η. The PDF form theoretically obtained from the FENE dumbbell model under Gaussian random flow in the absence of mean shear suggested that there was no range obeying an exponential form [18]. In the intermediate elongation range, theoretical studies [15–19] have suggested that $P(r_e)$ obeys a power law in the intermediate range $r_{eq} \ll r_e \ll R_0$ given by

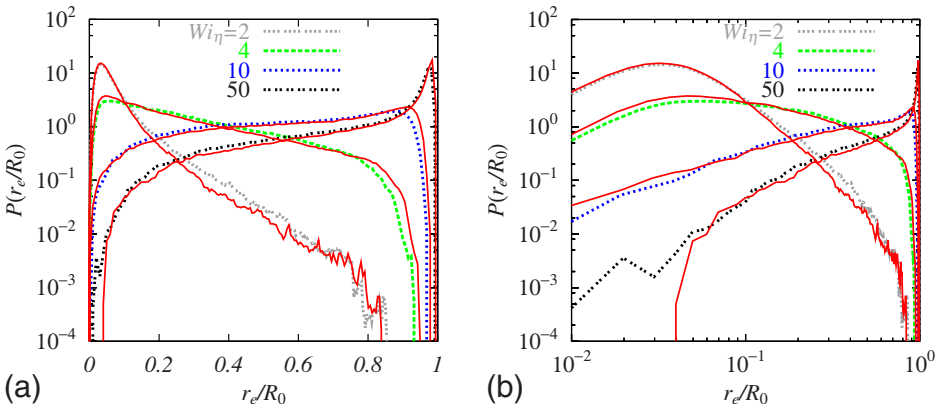

FIG. 9. (Color online) Comparison of the PDF forms between $N_b=20$ and $N_b=2$ (plotted by solid lines) for $\mathrm{Wi}_\eta=2$, 4, 10, and 50. The curves are same as those in Fig. 8 but plotted (a) on a semi-logarithmic scale and (b) on a double-logarithmic scale.

$$P(r_e) \sim r_e^{-1+\beta(\mathrm{Wi}_\eta)}, \tag{49}$$

where β depends on Wi_η and the spatial dimension. Figure 9(b) shows the double-logarithmic plot of Fig. 8(a), indicating that near power-law behavior occurred in the range $0.05 < r_e/R_0 < 0.2$. However, it is difficult to evaluate the scaling exponents because of the narrow scaling ranges in our results. The scaling behavior near the CS transition will be discussed later.

The CS transition can be clearly seen in the Wi_η dependence of the end-to-end distance moments. Figure 10 shows the variations of the mean value of end-to-end distances $\langle r_e \rangle$ and the standard deviation $\sigma_{r_e} = \sqrt{\langle r_e^2 \rangle - \langle r_e \rangle^2}$ divided by $\langle r_e \rangle$ (coefficient of variation $\sigma_{r_e}/\langle r_e \rangle$) with Wi_η for $N_b=20$ and $N_b=2$ cases. A coiled state was observed when $\mathrm{Wi}_\eta < 1$, while the mean end-to-end distance gradually increased with Wi_η, indicating that the polymer chain preferred to remain stretched when $\mathrm{Wi}_\eta \gg 1$. Signs of a transition were also observed for $\sigma_{r_e}/\langle r_e \rangle$ in the range $1 < \mathrm{Wi}_\eta < 5$, where the fluctuations around $\langle r_e \rangle$ rapidly increased. We note again that variation near the CS transition was insensitive to the number of beads when the parameter mapping of Eqs. (43) and (44) was used.

The CS transition was also observed in the dynamics of the end-to-end distance fluctuations. We evaluated the Wi_η

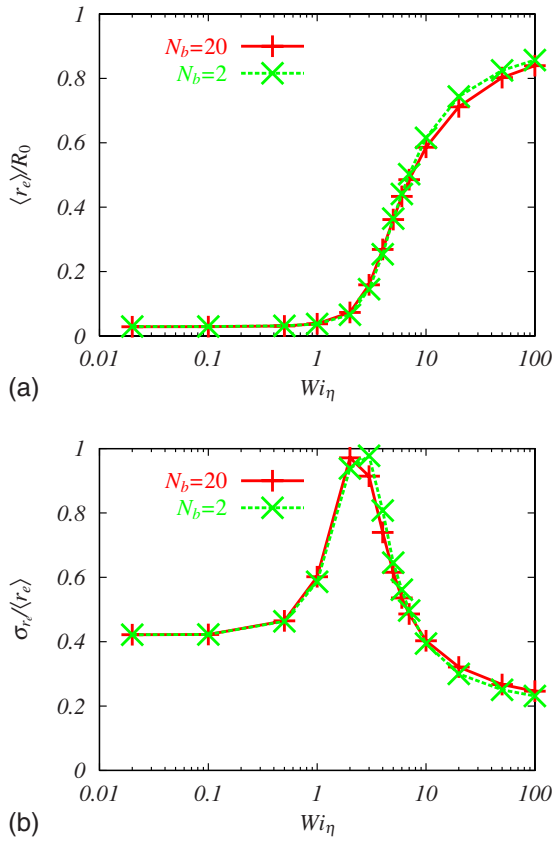

FIG. 10. (Color online) Wi_η dependence of the (a) mean end-to-end distance $\langle r_e \rangle$ and (b) coefficient of variation $\sigma_{r_e}/\langle r_e \rangle$ when $N_b=20$ and 2.

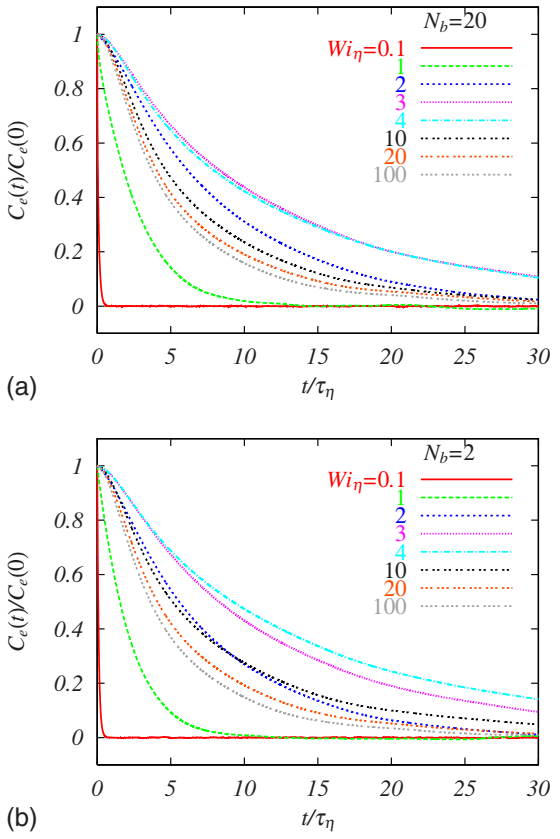

FIG. 11. (Color online) Autocorrealtion function of the end-to-end distance r_e for (a) $N_b=20$ and for (b) $N_b=2$ with Wi_η ranging from 0.1 to 100.

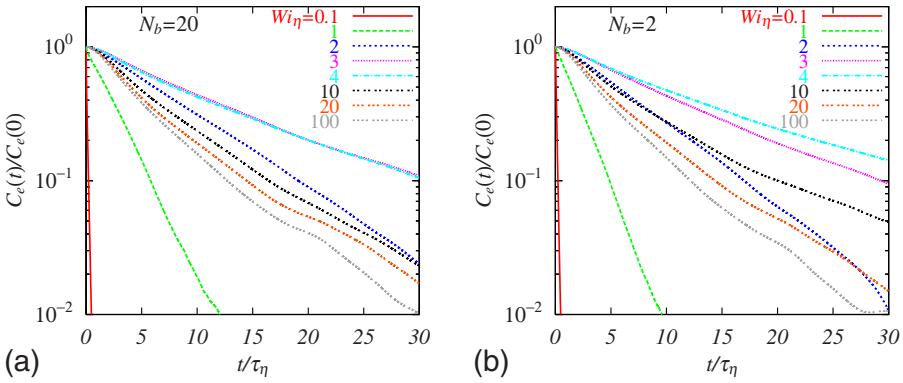

FIG. 12. (Color online) Same curves as in Fig. 11, but plotted on a semilogarithmic scale.

dependence of the temporal autocorrelation function of r_e, $C_e(t)=\langle[r_e(t)-\langle r_e\rangle][r_e(0)-\langle r_e\rangle]\rangle$, for $N_b=20$ and 2. Figure 11 shows the resulting curves. The correlation function decayed at slower rate when Wi_η was increased from 0.1 to 4. However, when $\mathrm{Wi}_\eta>4$, the decay rate of the correlation function was larger and the curve seemed to saturate when $\mathrm{Wi}_\eta=100$. These features were almost independent of the number of beads, as shown in the N_b dependence of the static properties. Figure 12 also shows the same curves in Fig. 11, but plotted on a semilogarithmic scale. The decay was approximately represented by an exponential function, although the statistical convergence of the tail of $C_e(t)$ was insufficient.

To evaluate the correlation time of the end-to-end distance fluctuation, we calculated the integral time from the autocorrelation function as $T_e=\int_0^\infty C_e(t)/C_e(0)dt$. T_e against Wi_η curves are shown in Fig. 13. The correlation time reached maximum value at about $12\tau_\eta$ $(14\tau_\eta)$ when $\mathrm{Wi}_\eta=3-4$ with $N_b=20$ $(N_b=2)$. This critical value was almost the same as that evaluated by the Wi_η dependence of the r_e moments. We see again that the detailed mechanism of the CS transition was insensitive to N_b, provided that the parameter mapping of Eqs. (43) and (44) was used.

The critical value of Wi_η at which the CS transition occurred was estimated from the governing equations for the end-to-end distance r_e. The equation of motion for $\boldsymbol{r}_e$ can be derived from Eq. (26) as

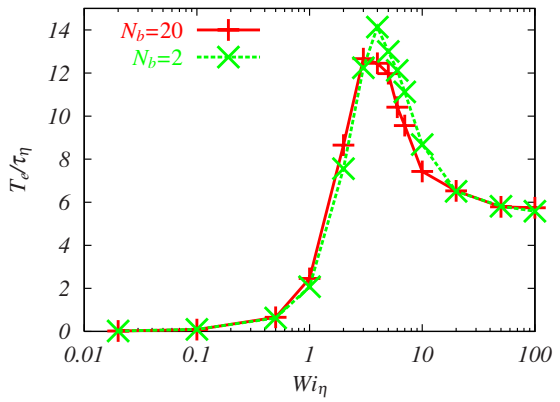

FIG. 13. (Color online) Variation of the integral time evaluated from the decay of the autocorrelation function of the end-to-end distance of the polymer chain against Wi_η for $N_b=20$ and 2.

$$\frac{d\boldsymbol{r}_e}{dt}=\boldsymbol{r}_e\cdot\nabla\boldsymbol{u}-\frac{1}{2\tau_s}\sum_{n=1}^{N_b-1}f_n\boldsymbol{r}^{(n)}+\frac{1}{4\tau_s}\sum_{n=1}^{N_b-1}(f_{n+1}\boldsymbol{r}^{(n+1)}+f_{n-1}\boldsymbol{r}^{(n-1)})+\frac{1}{\sqrt{\tau_s}}\boldsymbol{\xi}, \tag{50}$$

where $\boldsymbol{\xi}=(\boldsymbol{W}_N-\boldsymbol{W}_1)/\sqrt{2}$. To discuss the critical behavior around the CS transition, it is useful to linearize f_n of Eq. (50) as

$$\frac{d\boldsymbol{r}_e}{dt}=\boldsymbol{r}_e\cdot\nabla\boldsymbol{u}-\frac{1}{2\tau_s}\boldsymbol{r}_e+\boldsymbol{G}, \tag{51}$$

where $\boldsymbol{G}=(4\tau_s)^{-1}\Sigma_{n=1}^{N_b-2}(\boldsymbol{r}^{(n+1)}+\boldsymbol{r}^{(n)})+\boldsymbol{\xi}/\sqrt{\tau_s}$. This corresponds to the equation of motion for $\boldsymbol{r}_e$ derived from the Hookean polymer chain. Using Eq. (51), we can write the dynamics of the end-to-end distance r_e near the CS transition as

$$\frac{dr_e}{dt}=\left(\lambda(t)-\frac{1}{2\tau_s}\right)r_e+\boldsymbol{G}\cdot\hat{\boldsymbol{e}}, \tag{52}$$

where $\hat{\boldsymbol{e}}\equiv\boldsymbol{r}_e/r_e$ and

$$\lambda(t)\equiv\hat{e}_j\frac{\partial u_i}{\partial x_j}\hat{e}_i. \tag{53}$$

Equation (52) indicates that the polymer chain extension is governed by the dynamics of $\lambda(t)$. We call $\Lambda=\lambda-(2\tau_s)^{-1}$ the polymer extension rate. The mean polymer extension rate $\langle\Lambda\rangle$ measures the extent to which the polymer chain prefers to remain coiled $(\langle\Lambda\rangle<0)$ or stretched $(\langle\Lambda\rangle>0)$. This is similar to the condition expressed in terms of the Lyapunov exponent for particle dispersion [28,30]. This point will be discussed in Sec. VII. Figure 14 shows the curves $\langle\Lambda\rangle$ against Wi_η for $N_b=20$ and $N_b=2$ cases. We can confirm that $\langle\Lambda\rangle$ crossed zero when $3<\mathrm{Wi}_\eta<4$, indicating that the CS transition occurred in this range.

Further information on the CS transition point was gained by investigating the scaling behavior of the end-to-end distance PDF $P(r_e)$. Theoretical predictions [15–19] tell us that the scaling law of the polymer elongation PDF (49) at the CS transition is given by $\beta=0$, so we expect to observe $P(r_e)\sim r_e^{-1}$ at the point of CS transition. Figure 15 shows a double-logarithmic plot of $P(r_e)$ for the cases $\mathrm{Wi}_\eta=3$, 3.5, and 4 with $N_b=2$. Clearly, the curve for $\mathrm{Wi}_\eta=3.5$ was very close to the -1 law in the intermediate range. This suggests that the CS transition occurs in the range $3<\mathrm{Wi}_\eta<4$. It would be

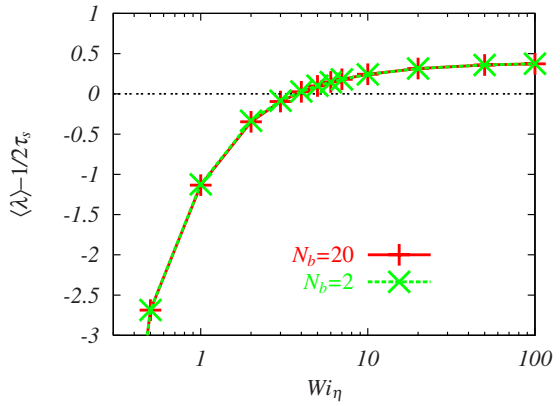

FIG. 14. (Color online) Curves for the mean polymer extension rate $\Lambda=\langle\lambda\rangle-1/2\tau_s$ against Wi_η for $N_b=20$ and 2.

interesting to study how the critical Wi_η value at the CS transition depends on turbulent flow properties such as the Reynolds number R_λ. This point will be discussed in a later section.

VI. RELATIONSHIP BETWEEN POLYMER ELONGATION AND VELOCITY GRADIENT DYNAMICS

In this section, we investigate the relationship between the polymer elongation and velocity gradient dynamics. Figure 16 compares the temporal fluctuations of the end-to-end distance $r_e(t)$ and $\lambda(t)$ along a trajectory of the same fluid particle when $\mathrm{Wi}_\eta=100$. $r_e(t)$ almost remained fully stretched state over a long period, only occasionally decreasing after $\lambda(t)$ reached a negative minimum value. To see this in more detail, zooms of the time series are also shown, indicating that the time lag between their minima was about $1.5\tau_\eta$. This fact implies that the states of λ determine the state of the polymer chain.

Let us further investigate the statistical nature of λ. The Wi_η effect on the PDF form of $\lambda(t)$ is shown in Fig. 17 for a bare PDF [Fig. 17(a)] and a normalized one [Fig. 17(b)]. The

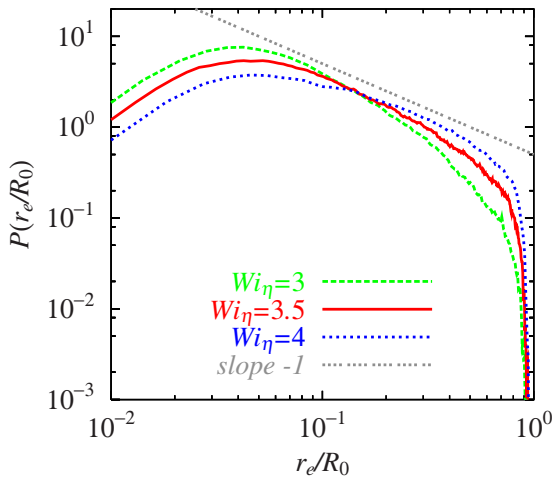

FIG. 15. (Color online) Scaling law of the PDF of the polymer end-to-end distance around the CS transition point obtained for the case $N_b=2$. The straight line shows the -1 slope.

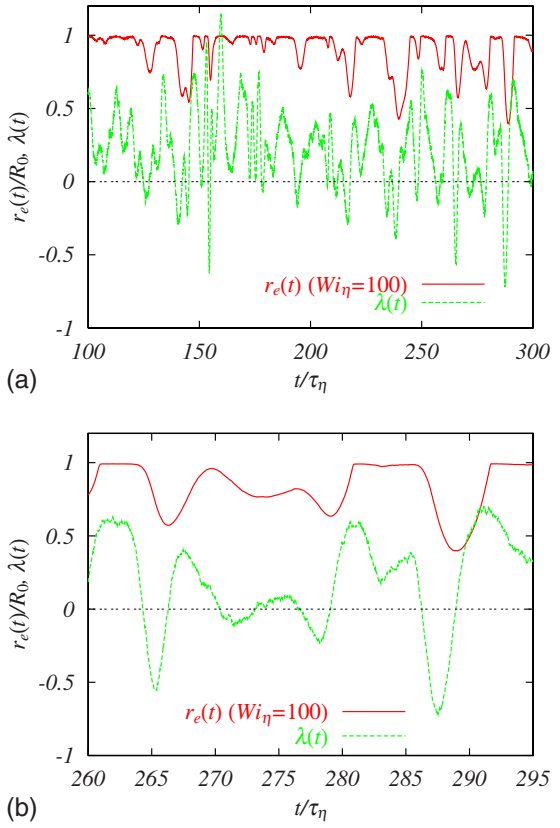

FIG. 16. (Color online) Comparison of the time series of r_e and λ, for which the temporal fluctuations were evaluated by $N_b=20$ along the trajectory of a single fluid particle. The lower figure (b) is a zoom of (a) in the region $260\leq t/\tau\leq 295$.

peak position of the PDF gradually increased with Wi_η, and the PDF form converged to a single curve for $\mathrm{Wi}_\eta\geq 10$. This implies that the dynamics of $\hat{\boldsymbol{e}}$ of an extended polymer chain were almost insensitive to the variation of Wi_η when $\mathrm{Wi}_\eta \gg 1$. It is remarkable that the PDF form when $\mathrm{Wi}_\eta \ll 1$ is very close to that of the longitudinal velocity gradient. In fact, λ is evaluated by

$$\lambda(t)=\hat{e}_j\frac{\partial u_i}{\partial x_j}\hat{e}_i=\frac{\delta u_L}{r_e}, \tag{54}$$

where $\delta u_L=[u_i(\boldsymbol{x}+\hat{\boldsymbol{e}}r_e/2)-u_i(\boldsymbol{x}-\hat{\boldsymbol{e}}r_e/2)]\hat{e}_i$ is the longitudinal component of the velocity difference vector along the direction of the end-to-end vector of the polymer chain. Equation (54) shows that λ equals the longitudinal velocity gradient in the limit $r_e\to 0$, suggesting that the PDF of λ approaches that of $\partial_1 u_1$ as Wi_η decreases. Although the bare PDF varied with Wi_η, as shown in Fig. 17(a), the normalized PDF plotted in Fig. 17(b) falls on the PDF curve of $\partial_1 u_1$ irrespective of Wi_η.

To observe the statistical dynamics of the temporal fluctuations of λ, we examined the autocorrelation function of λ, $C_\lambda(t)$, which is shown in Fig. 18. $C_\lambda(t)$ decayed more slowly for larger values of Wi_η and was constant when $\mathrm{Wi}_\eta\geq 10$. This accounted for the nature of the polymer orientation dynamics: the direction of the normalized end-to-end vector $\hat{\boldsymbol{e}}$ randomly varied with time due to the Brownian force when $\mathrm{Wi}_\eta<1$, while the direction of $\hat{\boldsymbol{e}}$ for $\mathrm{Wi}_\eta\geq 10$ was deter-

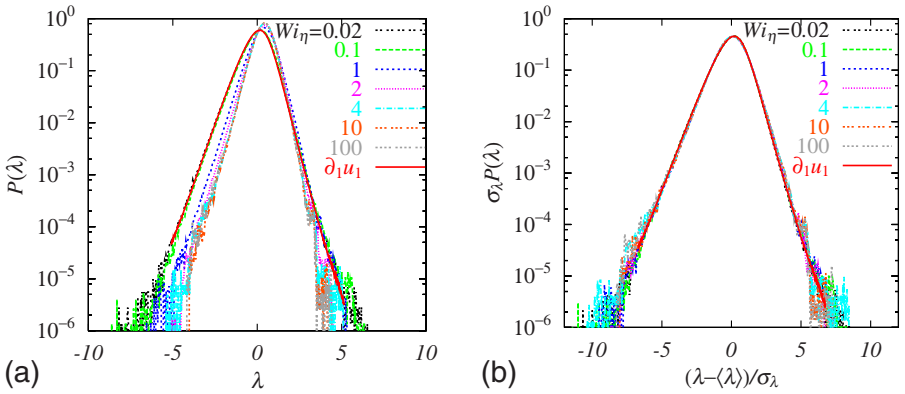

FIG. 17. (Color online) PDFs of $\lambda(t)$ fluctuation with $N_b=20$ for $\mathrm{Wi}_\eta=0.02-100$: (a) bare PDF and (b) normalized PDF. The solid lines in each plot are the PDFs for the longitudinal velocity gradient $\partial_1 u_1$.

mined by the rotational component of the velocity gradient. We also show the Wi_η effects on the correlation time T_λ of λ fluctuations in Fig. 19, along with the end-to-end distance T_e for comparison. T_λ algebraically increased with Wi_η for $\mathrm{Wi}_\eta<1$ and saturated to a constant value $T_\lambda\simeq 1.4\tau_\eta$ when $\mathrm{Wi}_\eta>1$. $T_\lambda\simeq 1.4\tau_\eta$ with $\mathrm{Wi}_\eta\gg 1$ was close to both the correlation time of S_{ij} ($T_S=2.1\tau_\eta$) and the time lag between the minima of r_e and λ shown in Fig. 16(b). This implied that the statistical nature of λ was governed by the rate of strain. In addition, T_λ was close to T_e when $\mathrm{Wi}_\eta<1$, suggesting that the Brownian random force dominated the evolution of r_e and $\hat{\boldsymbol{e}}$ in this parameter range. At the point of CS transition $\mathrm{Wi}_\eta=3-4$, T_e became much larger than T_λ. The disparity $T_e/T_\lambda\gg 1$ indicated critical polymer chain dynamics around the CS transition and suggested the possibility of constructing a probabilistic model for the end-to-end distance dynamics around the CS transition based on the probabilistic process of λ. Finally, we note once again that the curves obtained for $N_b=2$ had almost the same behavior as those for $N_b=20$, as shown in the plot of the PDF and autocorrelation function.

Next, we examine the statistical features of the alignment between the end-to-end vector $\boldsymbol{r}_e$ and the principal axis of the rate of strain tensor. The alignment statistics are characterized by the PDF of the inner product $\cos\theta_i=\boldsymbol{l}_i\cdot\hat{\boldsymbol{e}}$, where $\boldsymbol{l}_i$ $(i=1,2,3)$ represented the three eigenvectors belonging to the eigenvalues σ_i of the rate of strain tensor S_{ij}. λ is related to σ_i and $\cos\theta_i$ as $\lambda=\Sigma_{i=1}^{3}\sigma_i(\cos\theta_i)^2$ $(\sigma_1>\sigma_2>\sigma_3)$. Figure 20 shows PDFs of $\cos\theta_i$ for $i=1,2,3$ for $\mathrm{Wi}_\eta=0.2$ [Fig. 20(a)], 2 [Fig. 20(b)], and 20 [Fig. 20(c)], and for the vorticity alignment [Fig. 20(d)]. When $\mathrm{Wi}_\eta=0.2$, the PDF of each component was almost flat over the range $-1\le\cos\theta_i\le 1$, indicating that the end-to-end vector randomly took all orientations in time. Near the CS transition of $\mathrm{Wi}_\eta=2$, the PDFs for $\cos\theta_1$ and $\cos\theta_2$ had two peaks at ± 1, while those of $\cos\theta_3$ had a peak at zero, indicating that $\boldsymbol{r}_e$ tended to preferentially align in the $\boldsymbol{l}_1$ or $\boldsymbol{l}_2$ direction, with equal probability. As Wi_η increased, alignment along the $\boldsymbol{l}_2$ direction became most probable. This feature was insensitive to the variation of Wi_η as long as $\mathrm{Wi}_\eta>10$.

It is interesting to compare the curves in Fig. 20(c) to the case for the vorticity plotted in Fig. 20(d). This indicates that the alignment of the polymer chain in the $\boldsymbol{l}_2$ direction had a smaller probability than the probability of alignment of vorticity, even when Wi_η was larger than the critical value of the CS transition. The probability of polymer alignment along $\boldsymbol{l}_1$ is larger than that for the vorticity, suggesting that the polymer is more easily stretched than the vorticity. Recent studies of vorticity alignment [40] have shown that the vorticity aligns along the most extensional eigenvector of the *nonlocal* strain, which is defined by $S_{ij}^{NL}\equiv S_{ij}-S_{ij}^{L}$. The local strain $S_{ij}^{L}(\boldsymbol{x})$ is defined by Biot-Savart integration using the vorticity $\boldsymbol{\omega}(\boldsymbol{x}')$ within the finite integral range of the volume l^3, where l is an appropriate length scale. The study of [40] showed that strong vorticity stretching was due to S_{ij}^{NL}, where this is essentially a linear process. In the case of polymer stretching in this study, the polymer was passively advected by the

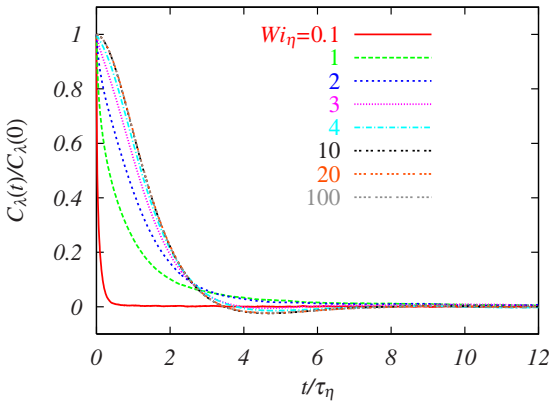

FIG. 18. (Color online) Lagrangian autocorrelation function of $\lambda(t)$ fluctuation with $N_b=20$ for $\mathrm{Wi}_\eta=0.1-100$.

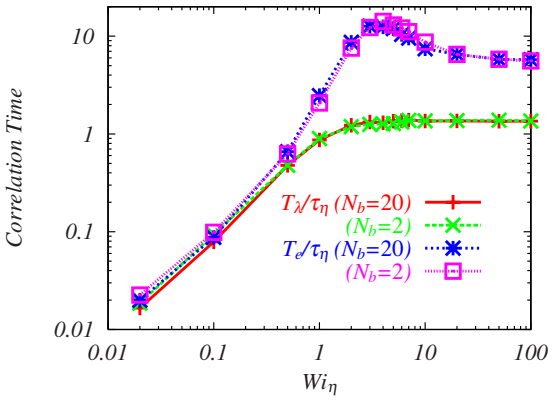

FIG. 19. (Color online) Comparison of the correlation time between the end-to-end distance T_e and λ fluctuation T_λ normalized by τ_η for various Wi_η's ranging from 0.02 to 100.

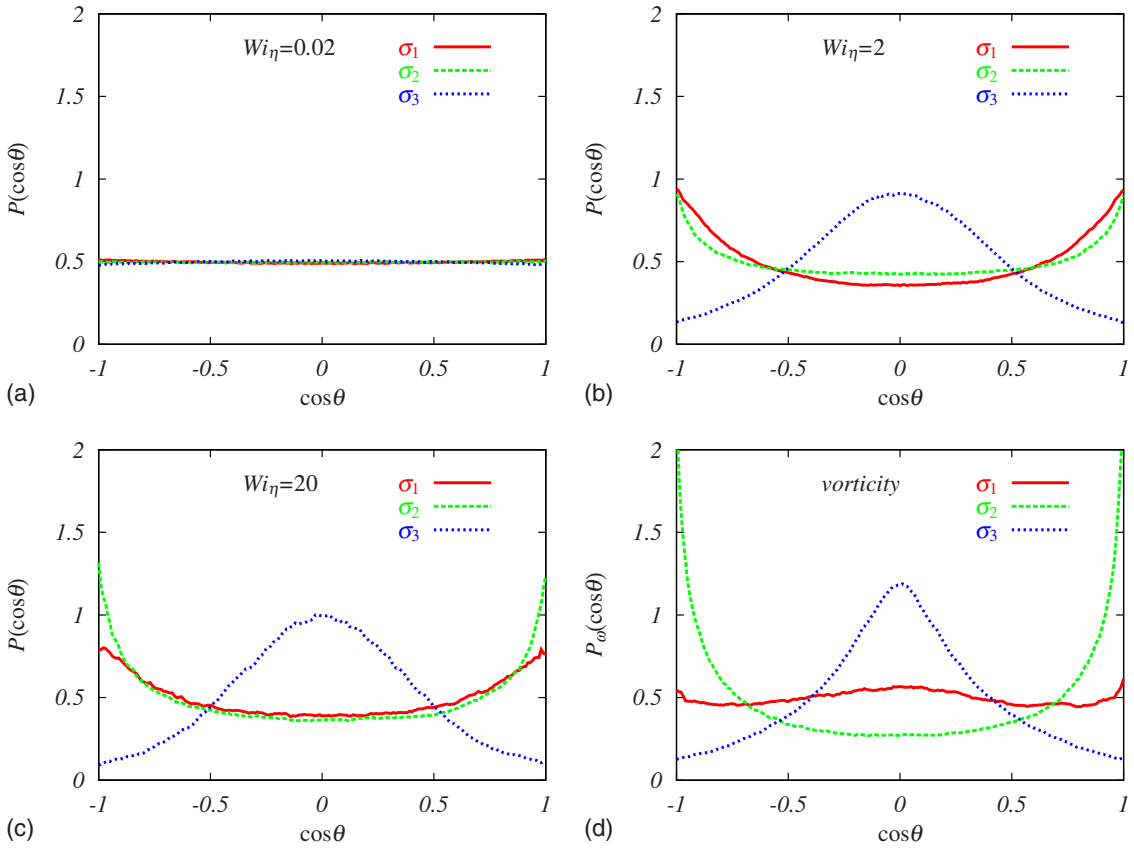

FIG. 20. (Color online) PDFs of the inner products of eigenvectors $\boldsymbol{l}_i$ of the rate of strain tensor and normalized end-to-end vector of the polymer chain (N_b=20) $\hat{\boldsymbol{e}}$, cos $\theta_i=\boldsymbol{l}_i\cdot\hat{\boldsymbol{e}}_i$, with i=1, 2, and 3 for Wi$_\eta$= (a) 0.2, (b) 2, and (c) 20, and (d) for the vorticity.

turbulent flow, so that this stretching mechanism was an essentially linear stretching by S_{ij}. This suggests that the polymer tended to align with the most extensional eigenvector. However, the alignment in the $\boldsymbol{l}_1$ direction was not significant for any Wi$_\eta$ values in these results. We infer that the alignment of the polymer at time t is strongly affected by the historical nature of the Lagrangian time evolution of the rate of strain tensor $S_{ij}(t')$ $(t'<t)$, because the polymer configuration is determined by the λ fluctuation with time lag $(\sim 1.5\tau_\eta)$, as shown in Fig. 16. It would be interesting to examine the effect of the historical nature of the velocity gradient fluctuation on polymer configuration and alignment properties, but this is beyond the scope of this paper.

Finally, we discuss the relationship between the polymer elongation and the topology of the local velocity gradient. The flow topologies of an incompressible flow can be classified by the eigenvalues of the velocity gradient tensor [41]. Eigenvalues α are obtained by the characteristic equation

$$\alpha^3 + Q\alpha + R = 0, \tag{55}$$

where Q and R are the tensor invariants given by

$$Q = -\tfrac{1}{2}\mathrm{tr}[(\boldsymbol{\nabla u})^2], \tag{56}$$

$$R = -\det(\boldsymbol{\nabla u}). \tag{57}$$

The discriminant $D=27R^2/4+Q^3$ determines the nature of the eigenvalues. There are three real distinct eigenvalues when $D<0$, while for $D>0$, there are one real and two complex-conjugate eigenvalues. For $D=0$, there are three real eigenvalues, of which two are equal. Moreover, we can classify the flow topology by the sign of Q, which is a measure of the difference between the rotation and strain motions. The local flow is dominated by rotation when $Q>0$, while $Q<0$ means that the strain is dominant in the local flow. These are summarized as follows:

(i) $D>0$, $R>0$: unstable focus/compressing;

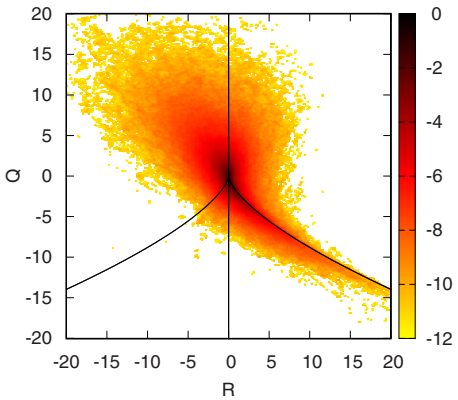

FIG. 21. (Color online) Joint PDF $P(Q,R)$ of the second and third invariants of the velocity gradient tensors Q and R. The solid curves in the figure represent R=0 and $D=27R^2/4+Q^3=0$, respectively. The color (grayscale) bar represents the value of ln $P(Q,R)$.

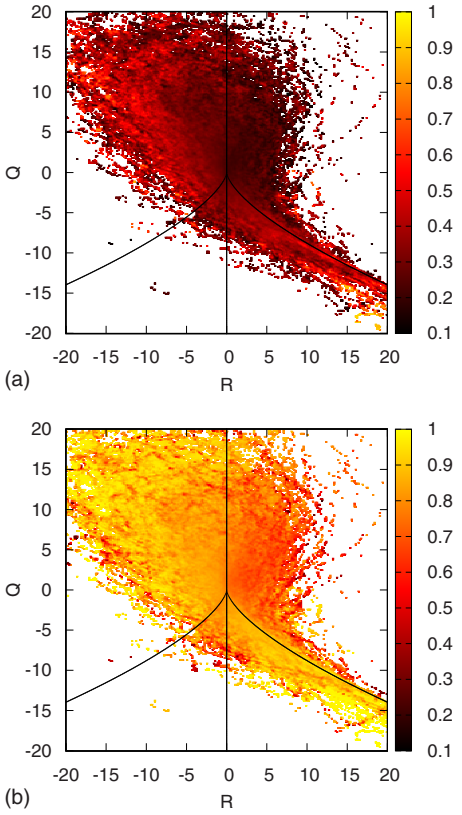

FIG. 22. (Color online) Mean polymer extension $\langle r_e/R_0|Q,R\rangle$ of the polymer chain (N_b=20) conditioned on the velocity gradient tensor invariants Q and R for (a) Wi_η=4 and (b) Wi_η=50. The color (grayscale) bar represents the value of $\langle r_e/R_0|Q,R\rangle$, and the solid curves in the figures represent R=0 and $D=27R^2/4+Q^3=0$.

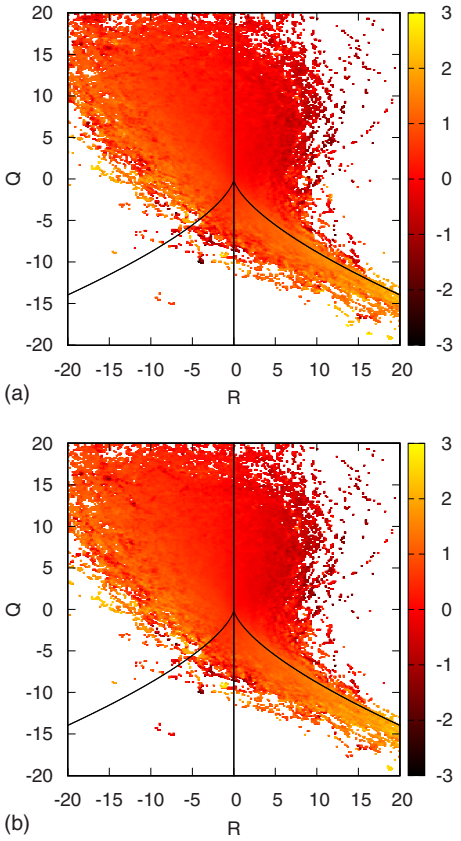

FIG. 23. (Color online) Mean value of λ for N_b=20 $\langle\lambda|Q,R\rangle$ conditioned on the velocity gradient tensor invariants Q and R for (a) Wi_η=4 and (b) Wi_η=50. The color (grayscale) bar represents the value of $\langle\lambda|Q,R\rangle$, and the solid curves in the figures represent R=0 and $D=27R^2/4+Q^3=0$.

(ii) $D>0$, $R<0$: stable focus/stretching;
(iii) $D<0$, $R>0$: unstable node/saddle/saddle; and
(iv) $D<0$, $R<0$: stable node/saddle/saddle.

The joint PDF of Q and R, $P(Q,R)$, is shown in Fig. 21, where the color bar represents the isosurface of $\ln P(Q,R)$. $\ln P(Q,R)$ has a characteristic "teardrop" shape, as found in previous studies [29,31].

To see the relationship between the polymer elongation and local flow topology, we calculated the mean polymer extension conditioned on Q and R, $\langle r_e/R_0|Q,R\rangle$. The results are shown in Fig. 22 for Wi_η=4 [Fig. 22(a)] and 50 [Fig. 22(b)]. We see that a larger extension of the polymer existed in regions of (ii) stable focus/stretching and (iii) unstable node/saddle/saddle when Wi_η=4. When Wi_η=50, the polymer chain had almost its largest extension in all regions except those of (i) unstable focus/compressing. These results indicate that the strongly extensional events of the polymer chain most likely corresponded to all regions except those of unstable focus/compressing ($D>0$ and $R>0$). These results using the polymer chain model (N_b=20) are generally consistent with preceding studies using the dumbbell model [29,31].

Figure 23 shows $\langle\lambda|Q,R\rangle$ conditioned on Q and R for Wi_η=4 [Fig. 23(a)] and Wi_η=50 [Fig. 23(b)]. λ had large positive values in regions of (ii) stable focus/stretching and (iii) unstable node/saddle/saddle irrespective of Wi_η, where the strongly stretching polymer was observed. Negative λ values occurred in the region of (i) unstable focus/compressing. The conditional statistics of λ were also less sensitive to the variation of Wi_η when $\mathrm{Wi}_\eta \geq 4$, as was seen in the behavior of the PDF of λ for various Wi_η's (Fig. 17).

VII. DISCUSSION AND CONCLUSION

We studied the dynamics of polymer stretching in isotropic turbulence using a multiscale computational approach. Homogeneous isotropic steady turbulence with an ensemble of polymers, modeled by beads connected by FENE springs, was directly simulated. The emphasis was on the statistical nature of the coil-stretch transition when the Weissenberg number Wi_η was changed. A CS transition at Wi_η between 3 and 4 was confirmed by the following facts: (i) the variance of the end-to-end vector of polymer chains had a maximum value; (ii) the PDF of the end-to-end distance obeyed a power-law decay with exponent −1 when Wi_η=3.5, consistent with previous studies; and (iii) the correlation time of the end-to-end polymer chain distance reached a maximum.

As shown in Fig. 16, the polymer stretching dynamics were governed by the behavior of λ. We discussed the similarities of the underlying physics between the polymer chain stretching dynamics and the pair dispersion of tracers initially close to each other. The statistical nature of the pair

dispersion of tracers has been characterized by analysis of the Lyapunov exponents. In a comprehensive DNS study of the Lyapunov exponents of tracers and heavy particles in HIT, it was found that $\lambda_1\tau_\eta=0.14-0.15$ when $R_\lambda=65-185$, where λ_1 is the mean value of the largest Lyapunov exponent for tracer dispersion [42]. It is interesting to note that $\langle\lambda\rangle\tau_\eta \simeq 0.13$ above the CS transition in this study ($R_\lambda=47$), suggesting that $\langle\lambda\rangle$ was approximated by λ_1. This observation is plausible given their similarities: the mechanism that increased the polymer chain end-to-end distance r_e was almost the same as that changing the distance among tracers, except that r_e was much larger.

In fact, it has been noted that the CS transition for the Hookean dumbbell model was determined by λ_1 for tracer dispersion and the relaxation time of the polymer τ_s, and the condition for the onset of CS transition was represented by $2\lambda_1\tau_s>1$ [15,16,28,30]. Interestingly, $2\langle\lambda\rangle\tau_s\simeq 0.92$ for $\mathrm{Wi}_\eta^c=3.5$, which is very close to unity. The value $2\lambda_1\tau_s=0.77\pm0.20$ was also obtained in an experimental study of single polymer dynamics in a random flow [20]. The relationship between the nature of the CS transition and the statistics of Lyapunov exponents indicates that the dependence of the CS transition point on the turbulence Reynolds number is closely related to how λ_1 varies with R_λ. The R_λ effect on $\lambda_1\tau_\eta$ obtained by [42], where $\lambda_1\tau_\eta$ slightly decreased from 0.15 to 0.14 as R_λ increased from 65 to 185, suggests that the CS transition point we observed for $R_\lambda=47$ was almost independent of R_λ for $R_\lambda<185$. It would be interesting in the future to study how the CS transition depends on the intensity of the turbulence or the degree of isotropy.

The statistical properties of the polymer dynamics studied were found to be insensitive to the variation of bead number N_b over a wide range of Wi_η, provided that the mapping formulas (43) and (44) proposed by Jin and Collins [32] were properly used. Generally, the bead number effects on the statistical nature of the polymer chain strongly depended on the flow properties and details of the mapping for the parameters r_{max} and τ_s [32].

When the Weissenberg number Wi_η was much larger, the polymer remained fully stretched along the extensional flow direction. This configuration, together with Eqs. (43) and (44), asymptotically yielded N_b-independent behavior of the polymer contribution to the elongation viscosity $(\bar{\mu}-3\overline{\mu_S})/nk_BT$ [43], where $\bar{\mu}$ and $\overline{\mu_S}$ are, respectively, the elongation and Newtonian solvent viscosities. This implied that the statistical nature of the polymer chain in the range $\mathrm{Wi}_\eta\gg 1$ was expected to be independent of N_b, as numerically tested in a preceding study [32].

However, when $\mathrm{Wi}_\eta\ll 1$, the effects of the velocity gradient fluctuation on polymer dynamics was negligibly small compared to the restoring and Brownian random forces. In this case, the polymer dynamics were governed by the elastic force of the linear spring and the random force such that

$$\frac{d\boldsymbol{x}^{(n)}}{dt}=\frac{1}{4\tau_s(N_b)}[\boldsymbol{x}^{(n+1)}+\boldsymbol{x}^{(n-1)}-2\boldsymbol{x}^{(n)}]+\frac{1}{\sqrt{2\tau_s(N_b)}}\boldsymbol{W}^{(n)}. \tag{58}$$

Applying a normal-mode decomposition to Eq. (58) yields the characteristic time scale of large-scale polymer deformation, the so-called the Rouse mode [44], in the limit $N_b\to\infty$,

$$\tau_R\sim\tau_s(N_b)N_b^2. \tag{59}$$

If the mapping formula (44) is applied to the scaling for $\tau_s(N_b)$, Eq. (59) tells us that the polymer dynamics with respect to the Rouse mode is almost independent of N_b when $N_b\gg 1$. Because the end-to-end vector dynamics of the polymer chain represents large-scale deformation governed by the Rouse mode, it is plausible that the statistical nature of $\boldsymbol{r}_e$ in the range $\mathrm{Wi}_\eta\ll 1$ is also independent of N_b.

The above facts suggest that the statistical nature of polymer chains is insensitive to the variation of bead number N_b, as long as we apply formulas (43) and (44) with $\mathrm{Wi}_\eta\ll 1$ and $\mathrm{Wi}_\eta\gg 1$. We have no theoretical basis with which to explain the N_b effect on the polymer chain dynamics in the range $\mathrm{Wi}_\eta=O(1)$. It will be vital in future theoretical studies to clarify the N_b effects on the critical dynamics of polymers around the CS transition.

Although our results for the bead number effect on polymer dynamics are only for two or 20 beads, if the insensitivity we have discovered is general, it will provide a useful way to study turbulence modification by performing two-way coupling simulations. The number of polymers necessary for the fluid to be modified is roughly estimated as $O(10^6)$ polymer chains per unit cell for DNS, for example, for Polyacrykamide ($M_p=18\times10^6$ amu) with 5 ppm polymer solution, we have $N_\eta=3.6\times10^6$ polymers per volume of η^3 ($\eta=2.8\times10^{-4}$ m at $R_\lambda\simeq 50$ estimated from the data in [13]). Hence, reducing the degrees of freedom of the polymer chains is vital. The number of degrees of freedom of a polymer is so small that we may reduce the computational cost of polymer model integration and introduce a large number of dumbbells into the flow field [31]. To make models with a low number of beads reliable for long polymer chains, it is necessary to study the same problem but with a large number of beads by incorporating the bending force, excluded volume force, and hydrodynamic interaction among beads into the model equations. It is further necessary to examine the effects of these additional forces on the statistical and dynamical nature of the polymer chain over wide range of values for Wi_η. This is an important challenge for future studies of polymer turbulence interaction.

ACKNOWLEDGMENTS

The authors thank V. Steinberg and R. Rubinstein for valuable remarks and corrections on the first version of the manuscript. T.W. and T.G.'s work was partially supported by Grants-in-Aid for Scientific Research No. 20760112 and No. 21360082, respectively, from the Ministry of Education, Culture, Sports, Science, and Technology of Japan. The authors also thank the Theory and Computer Simulation Center of the National Institute for Fusion Science for their computational support.

[1] J. L. Lumley, J. Polym. Sci. Macromol. Rev. **7**, 263 (1973).
[2] K. R. Sreenivasan and C. M. White, J. Fluid Mech. **409**, 149 (2000).
[3] A. Groisman and V. Steinberg, Nature (London) **405**, 53 (2000).
[4] T. Burghelea, E. Segre, and V. Steinberg, Phys. Rev. Lett. **96**, 214502 (2006).
[5] Y. Jun and V. Steinberg, Phys. Rev. Lett. **102**, 124503 (2009).
[6] E. S. G. Shaqfeh, Annu. Rev. Fluid. Mech. **28**, 129 (1996).
[7] A. Groisman and V. Steinberg, Nature (London) **410**, 905 (2001).
[8] T. Burghelea, E. Segre, and V. Steinberg, Phys. Rev. Lett. **92**, 164501 (2004).
[9] P. E. Arratia, C. C. Thomas, J. Diorio, and J. P. Gollub, Phys. Rev. Lett. **96**, 144502 (2006).
[10] M. Laso and H. C. Ottinger, J. Non-Newtonian Fluid Mech. **47**, 1 (1993).
[11] J. J. J. Gillissen, Phys. Rev. E **78**, 046311 (2008).
[12] S. Tamano, M. Itoh, S. Hotta, K. Yokota, and Y. Morinishi, Phys. Fluids **21**, 055101 (2009).
[13] N. T. Ouellette, H. Xu, and E. Bodenschatz, J. Fluid Mech. **629**, 375 (2009).
[14] P. G. De Gennes, J. Chem. Phys. **60**, 5030 (1974).
[15] M. Chertkov, Phys. Rev. Lett. **84**, 4761 (2000).
[16] E. Balkovsky, A. Fouxon, and V. Lebedev, Phys. Rev. Lett. **84**, 4765 (2000).
[17] J.-L. Thiffeault, Phys. Lett. A **308**, 445 (2003).
[18] M. M. Afonso and D. Vincenzi, J. Fluid Mech. **540**, 99 (2005).
[19] A. Celani, S. Musacchio, and D. Vincenzi, J. Stat. Phys. **118**, 531 (2005).
[20] S. Gerashchenko, C. Chevallard, and V. Steinberg, EPL **71**, 221 (2005).
[21] A. Celani, A. Puliafito, and D. Vincenzi, Phys. Rev. Lett. **97**, 118301 (2006).
[22] A. Celani, A. Puliafito, and K. Turitsyn, EPL **70**, 464 (2005).
[23] M. Chertkov, I. Kolokolov, V. Lebedev, and K. Turitsyn, J. Fluid Mech. **531**, 251 (2005).
[24] S. Gerashchenko and V. Steinberg, Phys. Rev. Lett. **96**, 038304 (2006).
[25] Y. Liu and V. Steinberg (unpublished).
[26] B. Eckhardt, J. Kronjager, and J. Schumacher, Comput. Phys. Commun. **147**, 538 (2002).
[27] G. Boffetta, A. Celani, and S. Musacchio, Phys. Rev. Lett. **91**, 034501 (2003).
[28] P. A. Stone and D. Graham, Phys. Fluids **15**, 1247 (2003).
[29] V. E. Terrapon, Y. Dubief, P. Moin, E. S. G. Shaqfeh, and S. K. Lele, J. Fluid Mech. **504**, 61 (2004).
[30] J. Davoudi and J. Schumacher, Phys. Fluids **18**, 025103 (2006).
[31] T. Peters and J. Schumacher, Phys. Fluids **19**, 065109 (2007).
[32] S. Jin and L. R. Collins, New J. Phys. **9**, 360 (2007).
[33] D. Vincenzi, S. Jin, E. Bodenschatz, and L. R. Collins, Phys. Rev. Lett. **98**, 024503 (2007).
[34] H. Yoshimoto and S. Goto, J. Fluid Mech. **577**, 275 (2007).
[35] J. P. L. C. Salazar, J. De Jong, L. Cao, S. H. Woodward, H. Meng, and L. R. Collins, J. Fluid Mech. **600**, 245 (2008).
[36] R. B. Bird, C. F. Curtiss, R. C. Amstrong, and O. Hassager, *Dynamics of Polymetric Liquids*, Kinetic Theory Vol. 2, 2nd ed. (Wiley, New York, 1987).
[37] T. Watanabe and T. Gotoh, J. Fluid Mech. **590**, 117 (2007).
[38] S. S. Girimaji and S. B. Pope, Phys. Fluids A **2**, 242 (1990).
[39] T. Gotoh, Y. Watanabe, Y. Shiga, T. Nakano, and E. Suzuki, Phys. Rev. E **75**, 016310 (2007).
[40] P. E. Hamlington, J. Schumacher, and W. J. A. Dahm, Phys. Fluids **20**, 111703 (2008).
[41] H. M. Blackburn, N. N. Mansour, and B. J. Cantwell, J. Fluid Mech. **310**, 269 (1996).
[42] J. Bec, L. Biferale, G. Boffetta, M. Cencini, S. Musacchio, and F. Toschi, Phys. Fluids **18**, 091702 (2006).
[43] J. M. Wiest and R. I. Tanner, J. Rheol. **33**, 281 (1989).
[44] M. Doi and S. F. Edwards, *The Theory of Polymer Dynamics* (Oxford University Press, New York, 1986).